

Gain-of-function p53 mutants co-opt chromatin pathways to drive cancer growth

Jiajun Zhu^{1,2,3}, Morgan A. Sammons^{1,2}, Greg Donahue^{1,2}, Zhixun Dou^{1,2}, Masoud Vedadi^{4,5}, Matthäus Getlik⁶, Dalia Barsyte-Lovejoy⁴, Rima Al-awar^{5,6}, Bryson W. Katona⁷, Ali Shilatifard⁸, Jing Huang⁹, Xianxin Hua⁷, Cheryl H. Arrowsmith^{4,10} & Shelley L. Berger^{1,2}

TP53 (which encodes p53 protein) is the most frequently mutated gene among all human cancers. Prevalent p53 missense mutations abrogate its tumour suppressive function and lead to a ‘gain-of-function’ (GOF) that promotes cancer. Here we show that p53 GOF mutants bind to and upregulate chromatin regulatory genes, including the methyltransferases *MLL1* (also known as *KMT2A*), *MLL2* (also known as *KMT2D*), and acetyltransferase *MOZ* (also known as *KAT6A* or *MYST3*), resulting in genome-wide increases of histone methylation and acetylation. Analysis of The Cancer Genome Atlas shows specific upregulation of *MLL1*, *MLL2*, and *MOZ* in p53 GOF patient-derived tumours, but not in wild-type p53 or p53 null tumours. Cancer cell proliferation is markedly lowered by genetic knockdown of *MLL1* or by pharmacological inhibition of the *MLL1* methyltransferase complex. Our study reveals a novel chromatin mechanism underlying the progression of tumours with GOF p53, and suggests new possibilities for designing combinatorial chromatin-based therapies for treating individual cancers driven by prevalent GOF p53 mutations.

Most mutant forms of p53 are caused by single amino acid substitutions mapping to the DNA-binding domain¹. These mutations result in expression of full-length p53 protein, but loss of wild-type (WT) tumour suppressive function^{2–4}. The high prevalence of missense substitutions, particularly certain ‘hotspot’ mutations, suggests a selective advantage during cancer progression. Indeed, these mutants gain neomorphic oncogenic functions, including altered cancer spectrum^{2,3}, deregulated metabolic pathways^{4,5}, increased metastasis^{6,7} and enhanced chemotherapy resistance⁸. Evidence from recent studies points to one potential mechanism of GOF p53, functioning through association with other transcription factors and driving gene transcription in oncogenic pathways, such as the mevalonate pathway⁴ and etoposide-resistance pathway⁸. A transcriptional mechanism is further supported by the importance of retaining an intact transactivation domain for oncogenic GOF p53 function^{4,9}. Nevertheless, how GOF p53 contributes to major changes of the cancer genome and transcriptome remains to be elucidated^{9,10}. Altered chromatin pathways have been implicated in various aspects of cancer^{11,12}, given their regulation of genome-wide transcription programs^{13,14}. However, to our knowledge, to date there has not been evidence of direct crosstalk between GOF p53 mutants and chromatin regulation.

Genome-wide binding of GOF p53 mutants

We carried out chromatin immunoprecipitation followed by sequencing (ChIP-seq) to determine genome-wide binding locations of p53 in a panel of breast cancer cell lines: MCF7 (wild-type p53), MDA-MB-175VII (wild-type p53), HCC70 (p53(R248Q)), BT-549 (p53(R249S)), and MDA-MB-468 (p53(R273H)). We found that the binding of p53 to gene-proximal regions (less than 10 kilobases (kb)) of transcription

start sites (TSS) in the two wild-type p53 cell lines strongly resembled each other, whereas these wild-type p53 peaks were highly dissimilar from the peaks in any of the GOF p53 mutants. Notably, p53 binding patterns in the three GOF p53 cell lines were similar when compared to each other (Fig. 1a and Extended Data Fig. 1a). In addition, we aligned published p53(R248W) ChIP-seq data from Li-Fraumeni syndrome (LFS) MDAH087 cells⁸, and again, TSS-proximal peaks of p53(R248W) resembled those of p53(R273H) and p53(R248Q) (Extended Data Fig. 1b, c), but were distinct from the wild-type p53 peaks (Extended Data Fig. 1d, e).

We performed motif analysis for TSS-proximal peaks of the p53(R273H) mutant that predicted the E26 transformation-specific (ETS) motif as the most enriched (Extended Data Fig. 2a), which is distinct from the wild-type p53 motif (Extended Data Fig. 2b). One ETS family member, ETS2, has been shown to consistently associate with mutant p53 (ref. 8). We confirmed that ETS2 interacts with various GOF p53 mutants, but interacts to a much lesser extent with wild-type p53 (Fig. 1b and Extended Data Fig. 2c), as previously noted⁸. Co-immunoprecipitation at endogenous protein levels also demonstrated that ETS2 interacts with GOF p53, but not with wild-type p53 (Extended Data Fig. 2d, e). We analysed ChIP-seq data sets from the ENCODE project for all transcription factors^{15,16}, and observed that, compared to other transcription factors, ETS family proteins have significantly higher overlap with GOF p53 TSS-proximal peaks, but not with wild-type p53 TSS-proximal peaks (Extended Data Fig. 2f, g). Notably, in both wild-type and GOF p53 cases, RNA polymerase II (Pol II) group has the highest percentage overlap with p53 peaks, indicative of transcriptional activity. The extent of Pol II overlap is similar to the ETS group in GOF p53 cells, but much higher than the ETS group in wild-type p53 cells (Extended Data Fig. 2f, g).

¹Cell and Developmental Biology, Perelman School of Medicine, University of Pennsylvania, Philadelphia, Pennsylvania 19104, USA. ²Epigenetics Program, Perelman School of Medicine, University of Pennsylvania, Philadelphia, Pennsylvania 19104, USA. ³Biomedical Graduate Studies, Perelman School of Medicine, University of Pennsylvania, Philadelphia, Pennsylvania 19104, USA. ⁴Structural Genomics Consortium, University of Toronto, Toronto, Ontario M5G 1L7, Canada. ⁵Department of Pharmacology and Toxicology, University of Toronto, Toronto, Ontario M5S 1A8, Canada. ⁶Drug Discovery Program, Ontario Institute for Cancer Research, Toronto, Ontario M5G 0A3, Canada. ⁷Abramson Family Cancer Research Institute, Department of Cancer Biology, Perelman School of Medicine, University of Pennsylvania, Philadelphia, Pennsylvania 19104, USA. ⁸Department of Biochemistry and Molecular Genetics, Feinberg School of Medicine, Northwestern University, 320 E. Superior Street, Chicago, Illinois 60611, USA. ⁹Cancer and Stem Cell Epigenetics, Laboratory of Cancer Biology and Genetics, Center for Cancer Research, National Cancer Institute, Bethesda, Maryland 20892, USA. ¹⁰Princess Margaret Cancer Centre, and Department of Medical Biophysics, University of Toronto, Toronto, Ontario M5G 2C4, Canada.

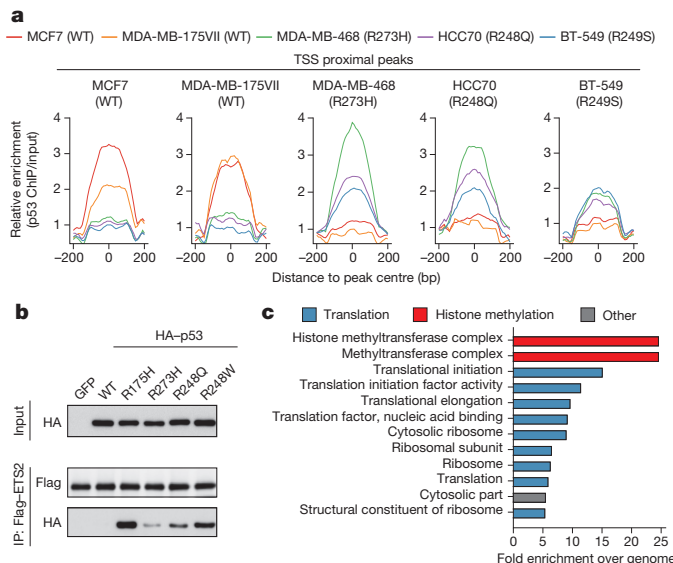


Figure 1 | Genome-wide binding of GOF p53 mutants. **a**, Area under the curve analysis showing p53 enrichment (ChIP/input) in five cell lines over TSS-proximal peak regions identified in each cell line. Mann–Whitney *U*-tests were performed to compute significance for combined wild-type (WT) and GOF p53 peaks: MCF7 ($P = 2.78 \times 10^{-6}$), MDA-MB-175VII ($P = 2.15 \times 10^{-4}$), MDA-MB-468 ($P < 2.2 \times 10^{-16}$), HCC70 ($P = 1.09 \times 10^{-3}$), BT-549 ($P = 3.7 \times 10^{-5}$). **b**, Co-immunoprecipitation of HEK293T cell-expressed Flag-ETS2 with *in vitro*-expressed GFP- or HA-tagged p53, followed by western blot. **c**, GO analysis of p53(R273H) TSS-proximal peaks (statistics are shown in Supplementary Table 1). Uncropped blots are in Supplementary Fig. 1.

GOF p53 targets chromatin regulators

To determine specific functional categories, we performed gene ontology (GO) analysis on TSS-proximal peaks. As expected, DNA damage response pathways were most enriched in wild-type p53 targets (Extended Data Fig. 2h and Supplementary Table 1). In contrast, p53(R273H) bound to genes related to translation and ribosomal synthesis (Fig. 1c and Supplementary Table 1), which was reasonable given the rapid growth rate of these cells. We were particularly intrigued by GOF p53 binding to a group of genes functionally related to histone methylation (Fig. 1c). This was seen in UCSC Genome Browser views at *MLL1* (*KMT2A*) and *MLL2* (*KMT2D*), genes encoding methyltransferases of histone H3 lysine 4 (H3K4) (Fig. 2a) that are components of alternative forms of the COMPASS complex (complex proteins associated with Set1). The other two GOF p53 mutants that we examined, as well as p53(R248W) from LFS MDAH087 cells⁸, all showed similar binding at *MLL1* and *MLL2* (Extended Data Fig. 3a, b, e, f). UCSC Genome Browser views confirmed binding of GOF p53 to a gene encoding a common subunit of COMPASS complexes, *RBBP5* (Extended Data Fig. 3h). In contrast, wild-type p53 did not appear to bind any of these genes, although as expected it bound promoter regions of its canonical targets, including *CDKN1A* (which encodes p21 protein), *MDM2* and *BBC3* (also known as *PUMA*) (Fig. 2a and Extended Data Fig. 3c, i, j). We then analysed a large set of 600 chromatin regulators for potential GOF p53 binding, and found an additional group of chromatin regulatory genes that showed peak enrichment (Supplementary Table 2). Of particular interest among these was *MOZ* (*KAT6A*), a histone acetyltransferase, and UCSC Genome Browser views confirmed the presence of GOF p53 but not wild-type p53 (Fig. 2a and Extended Data Fig. 3d, g).

Using ChIP-quantitative PCR (ChIP-qPCR), we validated the binding of GOF p53 to *MLL1*, *MLL2*, and *MOZ* genes, but not adjacently upstream or downstream of the peak regions (Fig. 2b and Extended Data Fig. 4a–c). Moreover, we confirmed GOF p53 binding to all other targets in the ‘histone methylation’ GO category (*RBBP5*, *OGT* and *PPP1CC*), and to a few additional chromatin factors

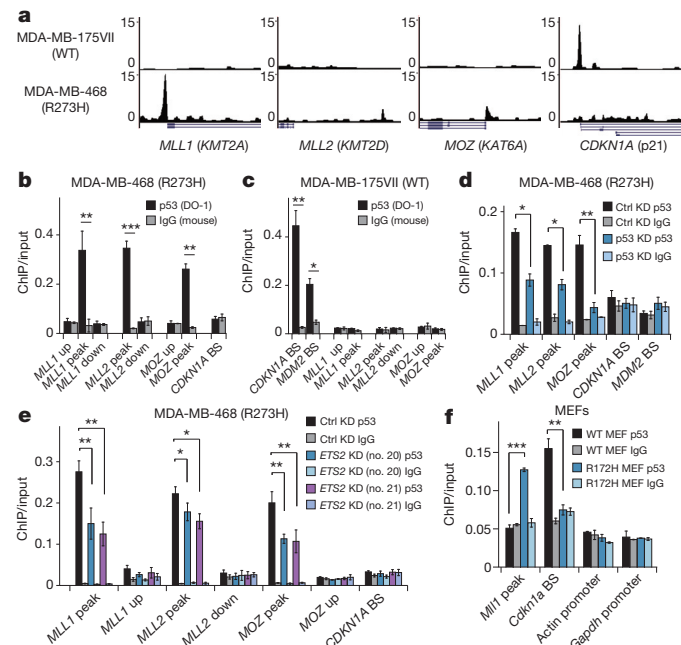


Figure 2 | GOF p53 mutants directly target chromatin regulators. **a**, UCSC Genome Browser views of p53 occupancy over promoter regions of *MLL1*, *MLL2*, *MOZ* and *CDKN1A*. **b**, **c**, ChIP-qPCR showing p53 or IgG enrichment (ChIP/input) in MDA-MB-468 (**b**) and MDA-MB-175VII (**c**) cells. BS, p53 binding site. Up, upstream of GOF p53 binding region; peak, GOF p53 binding region; down, downstream of GOF p53 binding region. A schematic of amplicon locations is shown in Extended Data Fig. 4a. **d**, **e**, ChIP-qPCR showing p53 enrichment changes upon reduction of p53 (**d**) or ETS2 (**e**) by shRNA-mediated knockdown. Numbers 20 and 21 denote two short hairpins, the sequences of which are shown in Supplementary Table 3. **f**, ChIP-qPCR showing p53 or IgG enrichment in MEFs bearing wild-type p53 or p53(R172H). Error bars represent mean \pm s.e.m.; $n = 3$; two-tailed Student’s *t*-test: * $P < 0.05$; ** $P < 0.01$; *** $P < 0.001$.

(including *SMARCD2* and *DCAF10*), in all three GOF p53 cell lines (Extended Data Fig. 4d–f). We verified the ChIP-qPCR results with a second p53 polyclonal antibody, FL393 (Extended Data Fig. 4g). In parallel experiments with both p53 antibodies, wild-type p53 showed binding to the *CDKN1A* and *MDM2* canonical binding sites, but not to any of the GOF p53 targets tested (Fig. 2c and Extended Data Fig. 4h). We also examined a pancreatic cancer cell line, PANC-1 (p53(R273H)), and observed a similar binding pattern (Extended Data Fig. 4i), suggesting a general phenomenon in various cancer types. Furthermore, the ChIP-qPCR signal of GOF p53 was attenuated upon p53 knockdown (Fig. 2d). Knockdown of *ETS2* also led to reduced binding of GOF p53 over *MLL1* and *MOZ*, and to a lesser extent, over the *MLL2* peak region (Fig. 2e). To test the association of GOF p53 near *MLL1* in a non-tumour background, we performed ChIP-qPCR in primary mouse embryonic fibroblasts (MEFs) with GOF p53 or wild-type p53, and consistently, mouse GOF p53 showed significant enrichment over the *MLL1* promoter region (Fig. 2f).

GOF p53 regulates MLL, MOZ, and histone modifications

To examine whether GOF p53 is required for expression of the chromatin regulators, we reduced GOF p53 levels in human cancer cells and found that the mRNA levels of *MLL1*, *MLL2* and *MOZ* were also decreased (Fig. 3a and Extended Data Fig. 5a); whereas no change was detected when the level of wild-type p53 was reduced (Extended Data Fig. 5b). Simply increasing wild-type p53 protein levels by stabilization mediated by the compound nutlin did not recapitulate activation of the chromatin regulators (Extended Data Fig. 5c, d). *MLL1* protein levels were also decreased in the GOF p53 knockdown (Fig. 3b), but not by wild-type p53 knockdown (Extended Data Fig. 5e), as was also observed for *MOZ* protein levels (Extended Data

Fig. 5f). Reduction of ETS2 levels led to decreased expression of *MLL1* and *MOZ*, and to a lesser extent, *MLL2* (Fig. 3c and Extended Data Fig. 5g), which was in accordance with the relative binding changes of GOF p53 to these genes (Fig. 2e). We verified the *ETS2* knockdown result in another GOF p53 cell line, BT-549, and detected similarly decreased expression of *MLL1* and *MOZ*, and to a lesser extent, *MLL2* (Extended Data Fig. 5h, i). We performed Pol II ChIP-qPCR and observed concomitantly decreased Pol II occupancy specifically over *MLL1*, *MLL2*, and *MOZ* TSS regions upon *ETS2* knockdown (Fig. 3d). We examined the importance of another ETS family member, *ETS1*. By contrast, *ETS1* knockdown had no effect on the expression of *MLL1*, *MLL2* or *MOZ* (Extended Data Fig. 5j, k), nor did it alter GOF p53 or Pol II binding (Extended Data Fig. 5l, m). As ETS family proteins consist of 28 members¹⁷, it is likely that additional ETS protein(s) other than *ETS1* may be involved. Nevertheless, our observations are consistent with previous studies showing that *ETS2*, but not *ETS1*, is important in mediating GOF p53 function^{8,18}.

The regulation of histone-modifying enzymes led to investigation of the cognate histone post-translational modifications (PTMs). We observed a global decrease in histone H3 lysine 9 acetylation (H3K9ac, catalysed by *MOZ*¹⁹) in response to knockdown of GOF p53, whereas other histone acetylation marks did not show notable changes (Fig. 3e and Extended Data Fig. 5n, o, p). The reduction of H3K9ac was also observed when the level of *MOZ* itself was decreased by short hairpin RNA (shRNA) (Extended Data Fig. 5q). In contrast, H3K4 tri-methylation and H3K4 mono-methylation (H3K4me3 and H3K4me1, catalysed by *MLL1* and *MLL2*, respectively²⁰) showed only a slight global reduction upon GOF p53 knockdown (Fig. 3e and Extended Data Fig. 5n, o, p). This is reasonable, however, given that H3K4 is methylated by six members of the COMPASS complexes²⁰, and previous studies showed that inhibiting or knocking one of them out did not substantially change global H3K4 methylation^{21,22}.

We further validated the regulation of *Mll1*, *Mll2*, and *Moz* by GOF p53 in the knock-in MEFs. We found significantly higher expression of these genes in GOF p53 MEFs than in wild-type p53 MEFs or in MEFs derived from p53 (gene *Trp53*) knockout mice (p53 null MEFs) (Fig. 3f and Extended Data Fig. 6a–c). Furthermore, when GOF p53 was reduced, *Mll1* expression was also lowered (Fig. 3g and Extended

Data Fig. 6d), and ectopically expressing GOF p53 in p53 null MEFs enhanced *Mll1* expression (Extended Data Fig. 6e, f). GOF p53 MEFs also showed higher global level of H3K9ac, and a slight elevation of H3K4me3, compared with wild-type p53 or p53 null MEFs (Fig. 3h and Extended Data Fig. 6g). Notably, other histone modifications associated with active gene transcription, including H3K27ac and H3K36me3, remained at comparable levels (Fig. 3h). In addition, H3K4me3 or H3K9ac did not change upon knockdown of wild-type p53 (Extended Data Fig. 6h), even though cell growth was increased as expected (Extended Data Fig. 6i). Together, these data suggest that changes in H3K4me3 and H3K9ac are specific to GOF p53 directly activating *MLL1* and *MOZ* enzymes.

The modest global change in H3K4me3 in the presence of GOF p53 prompted investigation of local changes in H3K4 methylation. We performed RNA-seq and H3K4me3 ChIP-seq in MEFs with endogenous wild-type p53 or GOF p53. Compared with the genome-wide average, known *MLL1* target genes²² were more highly expressed and displayed higher H3K4me3 enrichment in GOF p53 MEFs (Extended Data Fig. 6j). For example, we observed increased H3K4me3 level and RNA expression within the *Hoxa* gene cluster (Fig. 3i and Extended Data Fig. 6k), a well-studied target of *MLL1* and commonly upregulated in leukaemia^{23,24}. Conversely, wild-type p53 targets, such as *Cdkn1a*, showed decreased RNA expression and TSS-associated H3K4me3 in GOF p53 MEFs (Extended Data Fig. 6l). Notably, H3K4me3 enrichment at the TSS of genes in GOF p53 MEFs was slightly, but significantly higher at a genome-wide level than in wild-type p53 MEFs (Extended Data Fig. 6m), consistent with the slight global increase of H3K4me3 (Fig. 3h). We validated the H3K4me3 ChIP-seq and RNA-seq results by ChIP-qPCR and RT-qPCR, respectively, observing significantly higher H3K4me3 enrichment in GOF p53 MEFs, and higher expression of *Hox* genes, than in wild-type p53 or p53 null MEFs (Fig. 3j and Extended Data Fig. 6n).

MLL1 is essential for cancer phenotype of GOF p53

Previous studies have revealed that cells expressing GOF p53 rely on it for cell growth and survival^{25,26}. GOF p53 knockdown in cancer cells led to a strong decrease in cell proliferation (Extended Data Fig. 7a). By contrast, lowering of wild-type p53 levels resulted in elevated

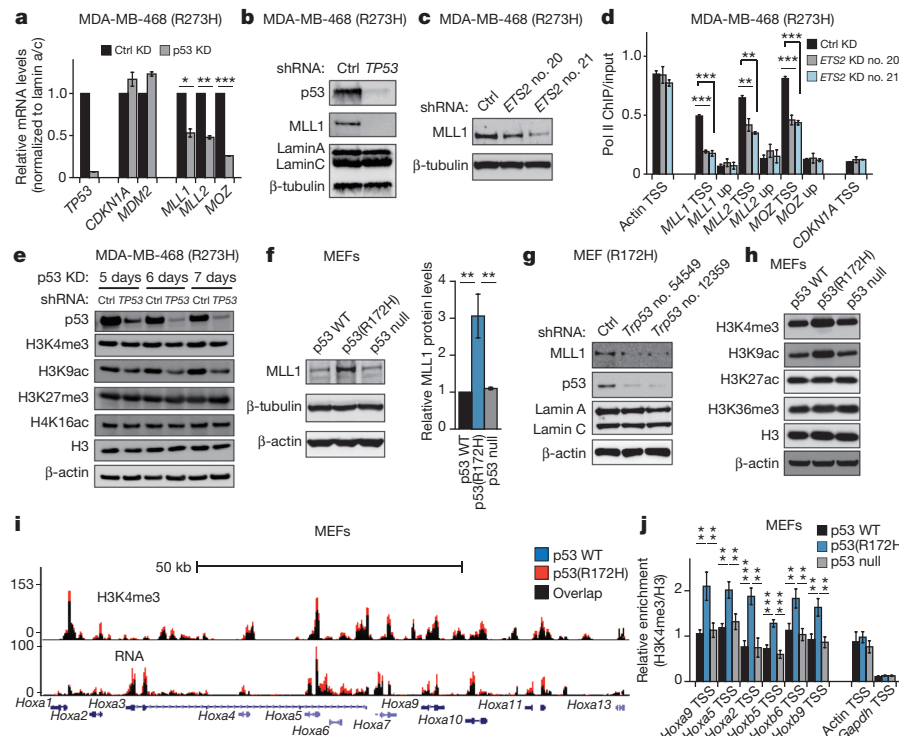


Figure 3 | GOF p53 mutants regulate MLL and MOZ and thereby histone post-translational modifications. **a**, RT-qPCR measuring mRNA level changes upon shRNA-mediated p53 knockdown. **b, c**, Western blot of MLL1 protein level changes upon p53 (b) or *ETS2* (c) knockdown. **d**, ChIP-qPCR showing Pol II enrichment changes upon shRNA-mediated *ETS2* knockdown. **e**, Western blot showing histone modification changes upon p53 knockdown over time. **f**, Western blot (left) and quantification (right) of endogenous MLL1 protein levels in MEFs with wild-type p53, p53(R172H) or p53 null. **g**, Western blot indicating MLL1 level changes upon p53 knockdown in MEFs with p53(R172H). Numbers 54549 and 12359 denote two short hairpins, sequences of which are shown in Supplementary Table 3. **h**, Western blot measuring endogenous histone modification levels in MEFs bearing wild-type p53, p53(R172H) or p53 null. **i**, Overlaid UCSC Genome Browser views of H3K4me3 and RNA levels in MEFs with p53 WT or R172H, over *Hoxa* gene cluster. **j**, ChIP-qPCR showing H3K4me3 enrichment (H3K4me3 ChIP/H3 ChIP) in MEFs with wild-type p53, p53(R172H) or p53 null. Uncropped blots are in Supplementary Fig. 1. Error bars represent mean \pm s.e.m.; $n = 3$; two-tailed Student's *t*-test; * $P < 0.05$; ** $P < 0.01$; *** $P < 0.001$.

growth (Extended Data Figs 6i and 7b). To investigate the function of GOF p53 driving chromatin regulators, we carried out the same time course, and found that the reduction of MLL1 or MLL2 in GOF p53 cancer cells led to a striking loss of cell growth (Extended Data Fig. 7c), phenocopying the knockdown of GOF p53 itself. By contrast, knockdown of *MLL1* or *MLL2* had a minimal effect on wild-type p53 cancer cells (Extended Data Fig. 7d, e).

We addressed the importance of this pathway to tumour-relevant phenotypes, first by examining the ability of cancer cells to form colonies. Reduction of MLL1 led to a decreased colony formation ability of MDA-MB-468 cells (p53(R273H)) (Fig. 4a and Extended Data Fig. 7f), but had little effect on the colony formation efficiency of MCF7 cells (wild-type p53) (Fig. 4b and Extended Data Fig. 7g). Similar results were observed in breast cancer cells BT-549 (p53(R249S)) and pancreatic cancer cells PANC-1 (p53(R273H)) (Extended Data Fig. 7h, i). We further confirmed the tumour formation phenotype in anchorage-independent growth assays in soft agar, showing that decreasing MLL1 specifically reduced the growth and colony size of GOF p53 cancer cells, but not wild-type p53 cancer cells (Extended Data Fig. 7j, k). We also investigated tumour growth on NOD-scid-gamma (NSG) immunodeficient mice. Knockdown of *MLL1* led to strongly reduced tumour formation ability in GOF p53 cells, as compared to GOF p53 cells with a non-targeting scrambled control knockdown (Fig. 4c, e). In contrast, *MLL1* knockdown did not alter the tumour formation ability of wild-type p53 cancer cells (Fig. 4d, e), again supporting a specific role for MLL1 in cancers with GOF p53, but not wild-type p53.

To further explore a critical role that these chromatin regulators may play in supporting growth of GOF p53 cells, and to rule out possible confounding factors in established cancer cell lines, we performed *Mll1* knockdown in the primary MEFs with knock-in GOF p53. Consistently, MLL1 reduction resulted in decreased proliferation of GOF p53 MEFs (Extended Data Fig. 8a). Importantly, re-expression of MLL1 in GOF p53 MEFs with p53 knockdown partially rescued the growth defects (Fig. 4f); partial rescue probably results from GOF p53 driving expression of multiple downstream targets, as described above. These results strongly indicate a direct role of MLL1, functioning

downstream of GOF p53 in maintaining proliferation of GOF p53 cells. We also performed *MLL1* knockdown (Extended Data Fig. 8b) in human non-cancer LFS cells—MDAH087 (p53(R248W)) and MDAH041 (p53 null²⁷; Extended Data Fig. 8c). Similar to the results obtained in cancer cells and in MEFs, *MLL1* knockdown reduced the growth rate of GOF p53 LFS cells (Fig. 4g and Extended Data Fig. 8d), again phenocopying the knockdown of GOF p53 itself (Extended Data Fig. 8e), but did not reduce the growth of either p53 null LFS cells (Fig. 4h and Extended Data Fig. 8f), nor primary non-cancer cells with wild-type p53 (IMR90 lung fibroblasts, Extended Data Fig. 8g, h). Re-expression of MLL1 again partially rescued the growth reduction by GOF p53 knockdown in LFS cells (Extended Data Fig. 8i). In addition, *MLL2* knockdown also decreased GOF p53 LFS cell proliferation, but not p53 null LFS cells (Extended Data Fig. 8j, k).

COMPASS inhibitors reduce GOF p53 cell growth

Chromatin regulators have emerged as promising targets of small molecule compounds in various human diseases including cancer^{11,28}. Menin is a scaffold protein of the COMPASS complex²⁰, directly interacting with the amino-terminal of MLL1^{29–31}, and is crucial for MLL1 activity and for maintenance of a subtype of leukaemia^{32,33}. We treated both GOF p53 and p53 null LFS cells with the previously reported menin antagonist, MI-2-2 (refs 34, 35). In agreement with the *MLL1* genetic knockdown experiments, MI-2-2 showed a dose-dependent inhibition of GOF p53 cell growth (Fig. 5a), but had very little effect on p53 null cells (Fig. 5b).

Recently, inhibition of MLL1 function has also been demonstrated by targeting its interaction with the WDR5 subunit of the COMPASS complex^{36,37}. As a second approach to pharmacological inhibition of MLL1 activity, we used OICR-9429, a newly characterized antagonist of interaction of WDR5 with MLL1 (ref. 38). This non-peptide, drug-like molecule binds to WDR5 in the MLL1 binding site of WDR5 ($K_d = 93 \pm 28$ nM), and disrupts the assembly of the WDR5/MLL1/RbBP5 complex in cells with half-maximum inhibitory concentration (IC_{50}) values below 1 μ M³⁸. In striking similarity to MI-2-2, we found a dose-dependent inhibition by OICR-9429 of GOF p53 LFS cell growth

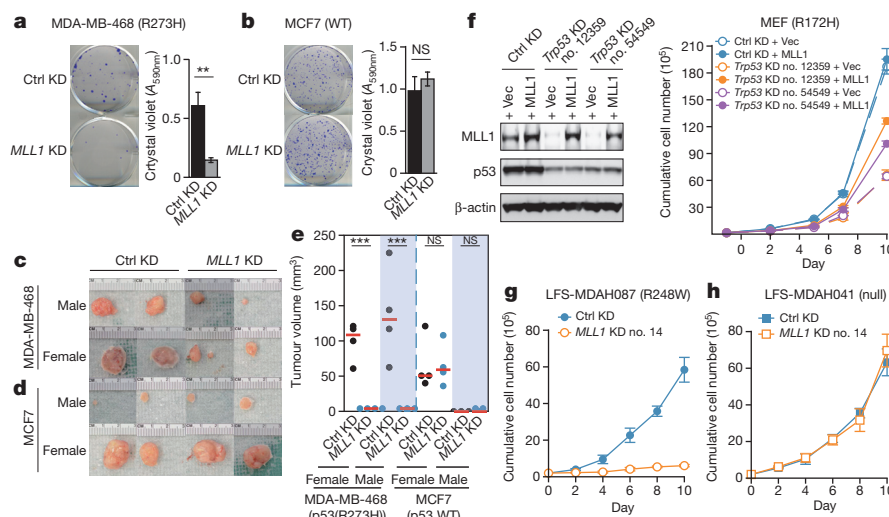


Figure 4 | *MLL1* knockdown reduces the proliferation and cancer phenotype of GOF p53 cells. **a, b**, Colony formation (left) and quantification (right) in MDA-MB-468 (**a**) or MCF7 (**b**) cells with non-targeting control (ctrl) or *MLL1* knockdown (KD). Two-tailed Student's *t*-test; ** $P < 0.01$; NS, $P > 0.05$; $n = 3$; the other two biological replicates are shown in Extended Data Fig. 7f, g. **c, d**, Excised xenograft tumours 20 weeks after NSG immunodeficient mice were subcutaneously injected with MDA-MB-468 (**c**) or MCF7 (**d**) cells carrying control or *MLL1* knockdown. Two representative images out of four total in each group are shown. **e**, Xenograft tumour volumes measured 10 weeks after initial injection described in **c** and **d**. Palpable tumours

at a size below 4 mm^3 were recorded as 4 mm^3 due to difficulties in measurement. Zeros indicate that the mouse did not have a palpable tumour. Red horizontal lines shown as average tumour volume of all four mice in each group. Mann-Whitney *U*-test; *** $P < 0.001$; NS, $P > 0.05$. **f**, Growth curve analysis and corresponding western blot in p53(R172H) MEFs with control or p53 knockdown, and vector control (Vec) or *MLL1* overexpression. **g, h**, Growth curve analysis in LFS MDAH087 (**g**) or MDAH041 (**h**) cells with control or *MLL1* knockdown. Uncropped blots shown in Supplementary Fig. 1. Error bars represent mean \pm s.e.m.; $n = 3$.

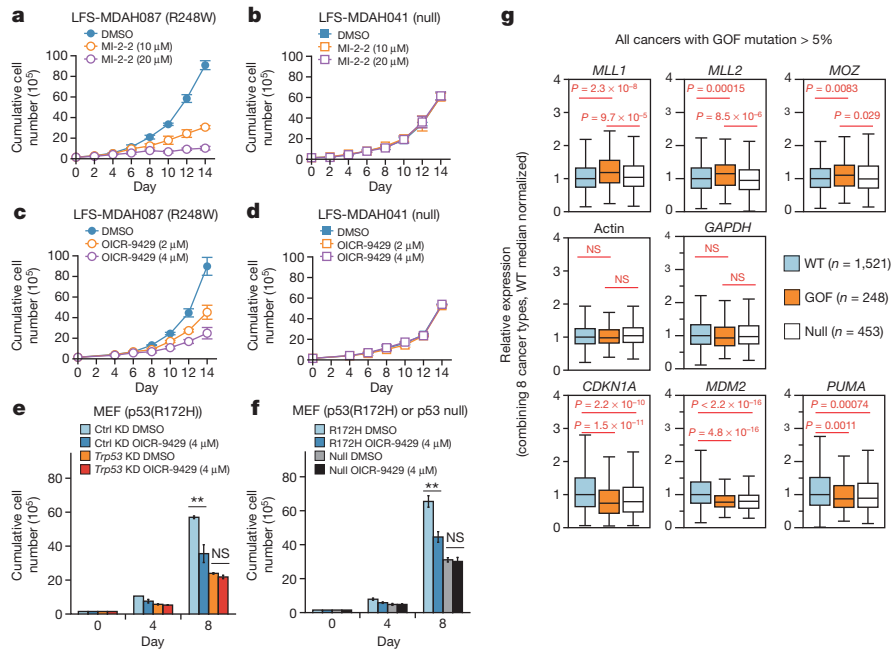


Figure 5 | COMPASS inhibitors specifically reduce GOF p53 cell growth. **a, b,** Growth curve analysis of LFS MDAH087 (**a**) and MDAH041 (**b**) cells treated with DMSO, and 10 μ M or 20 μ M Mi-2-2. **c, d,** Growth curve analysis of LFS MDAH087 (**c**) and MDAH041 (**d**) cells treated with DMSO, and 2 μ M or 4 μ M OICR-9429. **e,** Growth analysis of p53(R172H) MEFs carrying control or p53 knockdown, treated with DMSO or 4 μ M OICR-9429. **f,** Growth analysis of p53(R172H) or p53 null MEFs treated with DMSO or 4 μ M OICR-9429. **g,** Box plots of TCGA RNA expression profiles in tumours with wild-type p53, p53 GOF or p53 null. Mann–Whitney *U*-tests were performed to compute significance; NS, $P > 0.05$.

(Fig. 5c), and, again, little effect on p53 null LFS cells (Fig. 5d). Moreover, in the genetically controlled MEF cells, we observed similar results, that OICR-9429 specifically inhibits cell proliferation of GOF p53 MEFs (Fig. 5e, f), but not when GOF p53 is reduced (Fig. 5e) or in p53 null MEFs (Fig. 5f). These results provide strong evidence for a specific growth inhibitory effect of pharmacological drugs in targeting MLL COMPASS complex activity downstream of GOF p53.

We examined the significance of our findings in the context of human tumour samples, by analysing The Cancer Genome Atlas (TCGA). Based on p53 mutational status, we grouped tumour samples into: (1) wild type (no detectable p53 mutation); (2) GOF (missense mutation of R175H, R248Q, R248W, R249S or R273H); or (3) p53 null (p53 nonsense mutations or frameshift truncations). Tumours with other types of p53 mutations (other missense mutations, inframe insertion/deletion, or splicing mutations) were not included in further analysis, due to an unpredictable effect on the downstream chromatin regulators. We also focused our analysis on cancer types that include more than 5% of samples in the group comprising GOF p53. We first combined all samples from these cancer types, and observed significantly higher RNA expression of *MLL1*, *MLL2* and *MOZ* in GOF p53 tumours, compared to either wild-type p53 or p53 null tumours (Fig. 5g, top panels). As controls, expression levels of housekeeping genes including actin (*ACTB*) and *GAPDH* are consistent across the three groups (Fig. 5g, middle panels), whereas expression levels of wild-type p53 targets *CDKN1A*, *MDM2* and *PUMA* are significantly higher in the wild-type p53 group than the GOF p53 or p53 null group (Fig. 5g, lower panels). Next, we examined individual cancer types and observed similar gene expression patterns as the combination of all cancers (Extended Data Fig. 9a–f). Notably, given the heterogeneous population of tumour samples, and the small sample size of certain groups, not all pairwise comparisons are statistically significant, although the same trends always hold that GOF p53 tumours express higher levels of *MLL1*, *MLL2*, and *MOZ* than the other two groups. This is also true with canonical wild-type p53 targets, that is, although not all comparisons are statistically significant, the wild-type p53 groups always show higher levels of *CDKN1A*, *MDM2* and *PUMA* than the GOF p53 or p53 null tumour groups.

Discussion

Our results indicate that distinct prevalent GOF p53 mutants bind to a common newly identified group of gene targets genome-wide, to drive

expression of genes comprising a chromatin signature. The GOF p53 mapping occurs immediately associated with ETS motifs, and GOF p53 binds directly to ETS2, indicating that the substitutions in the DNA-binding domain of p53 unleash a latent interaction with ETS family transcription factors, as previously suggested⁸. Within this chromatin signature gene group targeted by GOF p53, the COMPASS methyltransferase pathway appears to be particularly well represented, but the new binding includes other chromatin regulators, such as the acetyltransferase *MOZ*. We find that expression of these modifying enzymes is dependent on GOF p53, which in turn elevates activating histone modifications, including H3K4me3 and H3K9ac. Our evidence points to MLL downstream pathways as key targets of GOF p53. Thus, as is the case in leukaemia bearing translocations of MLL, MLL pathways may contribute to GOF p53 oncogenic phenotypes and therefore cancer progression.

Importantly, our findings in both human cancer cells and LFS cells show that GOF p53 cells lose growth and tumour formation potential with similar timing kinetics upon knockdown of *MLL1* as they do with knockdown of GOF p53. A key comparison—to cancer and LFS cells that express wild-type p53 or are null for p53—shows very little response to *MLL1* knockdown. Hence, GOF p53 cells appear particularly dependent for growth on the MLL1 pathway. We provide further evidence of GOF p53 cell growth dependence on the COMPASS complex, by analysing cell sensitivity to two different pharmacological small compound inhibitors. These compounds target menin or WDR5 interaction with MLL1, and inhibit proliferation of LFS cells and MEFs expressing GOF p53 but not p53 null. The effects of the inhibitors are thus analogous to direct knockdown of *MLL1*. Hence, we conclude that a large cohort of GOF-p53-driven cancers, the growth of which was not previously known to be dependent on chromatin pathways, may be amenable to epigenetic therapeutics.

Online Content Methods, along with any additional Extended Data display items and Source Data, are available in the online version of the paper; references unique to these sections appear only in the online paper.

Received 24 June 2014; accepted 29 July 2015.

Published online 2 September 2015.

- Lawrence, M. S. *et al.* Discovery and saturation analysis of cancer genes across 21 tumour types. *Nature* **505**, 495–501 (2014).
- Lang, G. A. *et al.* Gain of function of a p53 hot spot mutation in a mouse model of Li–Fraumeni syndrome. *Cell* **119**, 861–872 (2004).

3. Olive, K. P. *et al.* Mutant p53 gain of function in two mouse models of Li-Fraumeni syndrome. *Cell* **119**, 847–860 (2004).
4. Freed-Pastor, W. A. *et al.* Mutant p53 disrupts mammary tissue architecture via the mevalonate pathway. *Cell* **148**, 244–258 (2012).
5. Zhang, C. *et al.* Tumour-associated mutant p53 drives the Warburg effect. *Nat. Commun.* **4**, 2935 (2013).
6. Subramanian, M. *et al.* A mutant p53/let-7i-axis-regulated gene network drives cell migration, invasion and metastasis. *Oncogene* **34**, 1094–1104 (2015).
7. Weissmueller, S. *et al.* Mutant p53 drives pancreatic cancer metastasis through cell-autonomous PDGF receptor β signaling. *Cell* **157**, 382–394 (2014).
8. Do, P. M. *et al.* Mutant p53 cooperates with ETS2 to promote etoposide resistance. *Genes Dev.* **26**, 830–845 (2012).
9. Scian, M. J. *et al.* Modulation of gene expression by tumor-derived p53 mutants. *Cancer Res.* **64**, 7447–7454 (2004).
10. Garritano, S., Inga, A., Gemignani, F. & Landi, S. More targets, more pathways and more clues for mutant p53. *Oncogenesis* **2**, e54 (2013).
11. Dawson, M. A. & Kouzarides, T. Cancer epigenetics: from mechanism to therapy. *Cell* **150**, 12–27 (2012).
12. Tam, W. L. & Weinberg, R. A. The epigenetics of epithelial-mesenchymal plasticity in cancer. *Nature Med.* **19**, 1438–1449 (2013).
13. Kouzarides, T. Chromatin modifications and their function. *Cell* **128**, 693–705 (2007).
14. Li, B., Carey, M. & Workman, J. L. The role of chromatin during transcription. *Cell* **128**, 707–719 (2007).
15. The ENCODE Project Consortium. An integrated encyclopedia of DNA elements in the human genome. *Nature* **489**, 57–74 (2012).
16. Gertz, J. *et al.* Distinct properties of cell-type-specific and shared transcription factor binding sites. *Mol. Cell* **52**, 25–36 (2013).
17. Hollenhorst, P. C., McIntosh, L. P. & Graves, B. J. Genomic and biochemical insights into the specificity of ETS transcription factors. *Annu. Rev. Biochem.* **80**, 437–471 (2011).
18. Xiong, S. *et al.* Pla2g16 phospholipase mediates gain-of-function activities of mutant p53. *Proc. Natl Acad. Sci. USA* **111**, 11145–11150 (2014).
19. Voss, A. K., Collin, C., Dixon, M. P. & Thomas, T. Moz and retinoic acid coordinately regulate H3K9 acetylation, Hox gene expression, and segment identity. *Dev. Cell* **17**, 674–686 (2009).
20. Shilatifard, A. The COMPASS family of histone H3K4 methylases: mechanisms of regulation in development and disease pathogenesis. *Annu. Rev. Biochem.* **81**, 65–95 (2012).
21. Cao, F. *et al.* Targeting MLL1 H3K4 methyltransferase activity in mixed-lineage leukemia. *Mol. Cell* **53**, 247–261 (2014).
22. Wang, P. *et al.* Global analysis of H3K4 methylation defines MLL family member targets and points to a role for MLL1-mediated H3K4 methylation in the regulation of transcriptional initiation by RNA polymerase II. *Mol. Cell. Biol.* **29**, 6074–6085 (2009).
23. Milne, T. A. *et al.* MLL targets SET domain methyltransferase activity to Hox gene promoters. *Mol. Cell* **10**, 1107–1117 (2002).
24. Nakamura, T. *et al.* ALL-1 is a histone methyltransferase that assembles a supercomplex of proteins involved in transcriptional regulation. *Mol. Cell* **10**, 1119–1128 (2002).
25. Lim, L. Y., Vidnovic, N., Ellisen, L. W. & Leong, C. O. Mutant p53 mediates survival of breast cancer cells. *Br. J. Cancer* **101**, 1606–1612 (2009).
26. Alexandrova, E. M. *et al.* Improving survival by exploiting tumour dependence on stabilized mutant p53 for treatment. *Nature* **532**, 352–356 (2015).
27. Zhu, Q., Wani, G., Wani, M. A. & Wani, A. A. Human homologue of yeast Rad23 protein A interacts with p300/cyclic AMP-responsive element binding (CREB)-binding protein to down-regulate transcriptional activity of p53. *Cancer Res.* **61**, 64–70 (2001).
28. Dawson, M. A., Kouzarides, T. & Huntly, B. J. Targeting epigenetic readers in cancer. *N. Engl. J. Med.* **367**, 647–657 (2012).
29. Huang, J. *et al.* The same pocket in menin binds both MLL and JUND but has opposite effects on transcription. *Nature* **482**, 542–546 (2012).
30. Yokoyama, A. *et al.* Leukemia proto-oncoprotein MLL forms a SET1-like histone methyltransferase complex with menin to regulate Hox gene expression. *Mol. Cell. Biol.* **24**, 5639–5649 (2004).
31. Caslini, C. *et al.* Interaction of MLL amino terminal sequences with menin is required for transformation. *Cancer Res.* **67**, 7275–7283 (2007).
32. Thiel, A. T., Huang, J., Lei, M. & Hua, X. Menin as a hub controlling mixed lineage leukemia. *Bioessays* **34**, 771–780 (2012).
33. Yokoyama, A. *et al.* The menin tumor suppressor protein is an essential oncogenic cofactor for MLL-associated leukemogenesis. *Cell* **123**, 207–218 (2005).
34. Grembecka, J. *et al.* Menin-MLL inhibitors reverse oncogenic activity of MLL fusion proteins in leukemia. *Nature Chem. Biol.* **8**, 277–284 (2012).
35. Shi, A. *et al.* Structural insights into inhibition of the bivalent menin-MLL interaction by small molecules in leukemia. *Blood* **120**, 4461–4469 (2012).
36. Karatas, H. *et al.* High-affinity, small-molecule peptidomimetic inhibitors of MLL1/WDR5 protein–protein interaction. *J. Am. Chem. Soc.* **135**, 669–682 (2013).
37. Karatas, H., Townsend, E. C., Bernard, D., Dou, Y. & Wang, S. Analysis of the binding of mixed lineage leukemia 1 (MLL1) and histone 3 peptides to WD repeat domain 5 (WDR5) for the design of inhibitors of the MLL1–WDR5 interaction. *J. Med. Chem.* **53**, 5179–5185 (2010).
38. Grebien, F. *et al.* Pharmacological targeting of the Wdr5-MLL interaction in C/EBP α N-terminal leukemia. *Nature Chem. Biol.* **11**, 571–579 (2015).

Supplementary Information is available in the online version of the paper.

Acknowledgements We thank M. Tainsky for the LFS cell lines; A. Weller, J. Glover and the Stem Cell and Xenograft Core at the University of Pennsylvania for help with the tumour xenograft experiments. S.L.B. is supported by NIH grant R01 CA078831. M.A.S. is supported by a Postdoctoral Fellowship from the American Cancer Society. X.H. is supported in part by a pilot grant from ITMAT of the University of Pennsylvania. A.S. is supported by NIH grant R01 GM069905. The Structural Genomics Consortium is a registered charity (number 1097737) that receives funds from AbbVie, Bayer, Boehringer Ingelheim, Genome Canada through the Ontario Genomics Institute (OGI-055), GlaxoSmithKline, Janssen, Lilly Canada, Merck, the Novartis Research Foundation, the Ontario Ministry of Economic Development and Innovation, Pfizer, Takeda, and the Wellcome Trust (092809/Z/10/Z). Funding was also provided to C.H.A. from the Canadian Cancer Society Research Institute.

Author Contributions J.Z. and S.L.B. initiated and led the project. J.Z., M.A.S., Z.D. and S.L.B. designed the experiments and interpreted the data. J.Z. and M.A.S. performed the experiments. J.Z., M.A.S. and G.D. analysed all next-generation sequencing data. M.V., M.G., D.B.-L., R.A. and C.H.A. developed OICR9429. B.W.K. and X.H. contributed to the use of menin inhibitor. A.S. and J.H. contributed to reagents used in this study. J.Z., M.A.S., C.H.A. and S.L.B. composed the manuscript. All authors reviewed and commented on the manuscript.

Author Information ChIP-seq and RNA-seq data can be accessed through NCBI Gene Expression Omnibus (GEO) database under accession number GSE59176. Reprints and permissions information is available at www.nature.com/reprints. The authors declare competing financial interests: details are available in the online version of the paper. Readers are welcome to comment on the online version of the paper. Correspondence and requests for materials should be addressed to S.L.B. (bergers@upenn.edu).

METHODS

Data reporting. No statistical methods were used to predetermine sample size. The experiments were not randomized. The investigators were not blinded to allocation during experiments and outcome assessment.

Cell culture. MCF7, MDA-MB-175VII, HCC70, BT-549, and MDA-MB-468 cell lines were obtained from American Type Culture Collection (ATCC), and were cultured in a 37 °C incubator at 20% oxygen, in standard tissue culture medium (DMEM with 10% FBS, 100 units per ml penicillin and 100 µg per ml streptomycin) supplied with non-essential amino acids. Li-Fraumeni Syndrome cell lines MDAH087 and MDAH041 were obtained from Michael A. Tainsky (Wayne State University, Detroit, MI) as a gift, and were cultured in a 37 °C incubator at 3% oxygen, in standard tissue culture medium. R172H knock-in mice were generated by Tyler Jacks (Massachusetts Institute of Technology)³ and obtained from the NCI Mouse Repository. Primary MEFs from 13.5-day embryos were generated as previously described³⁹, and cultured in standard tissue culture medium in a 37 °C incubator at 3% oxygen condition.

Western blot and antibodies. Cells were lysed in modified RIPA buffer containing 150 mM NaCl, 1% NP-40, 50 mM Tris-Cl, pH 8.0, and 1% SDS, supplemented with protease inhibitors (Life Technologies, number 78446) before use. Protein concentration was determined by BCA protein assay (Life Technologies, number 23227), following which equal amount of proteins were loaded and separated in polyacrylamide gels. Proteins were then transferred to nitrocellulose membrane. Antibodies used in this study were as follows: p53 monoclonal antibody DO-1 (Calbiochem EMD); p53 polyclonal antibody FL393 (Santa Cruz Biotechnology, sc-6243). Flag (Sigma, M2, F1804), HA (Rockland, 600-401-384), histone H3 (abcam, ab1791), H3K4me1 (abcam, ab8895), H3K4me2 (Active Motif, 39142), H3K4me3 (abcam, ab8580), H3K9ac (Active Motif, 39137), H3K14ac (Active Motif, 39616), H3K27ac (abcam, ab4729), H3K36me3 (abcam, ab9050), ETS2 (Santa Cruz Biotechnology, sc-351), MLL1 (Bethyl Laboratories, A300-086A), MOZ (Novus Biologicals, 21620002), mouse p53 antibody for ChIP experiments (Santa Cruz Biotechnology, sc-1312 (M-19)), mouse p53 antibody for western blot analysis (Cell Signaling Technology, number 2524), RNA polymerase II (abcam, ab817).

Co-immunoprecipitation. Flag tagged ETS2 protein was transfected (Life Technologies, number 11668019) and expressed in HEK293T cells and then subjected to immunoprecipitation with Flag antibody conjugated protein G Dynabeads (Life Technologies, number 10004D). Following stringent washes, HA-tagged wild-type p53 or GOF p53 (generated by *in vitro* translation (Thermo, number 88881)) was added to co-immunoprecipitate with Flag-ETS2 in buffer containing: 20 mM Tris, pH 8.0, 137 mM NaCl, 1 mM MgCl₂, 1 mM CaCl₂, 1% NP-40, and protease inhibitors. Endogenous co-immunoprecipitation experiments were performed in buffer containing: 20 mM Tris, pH 8.0, 137 mM NaCl, 1 mM MgCl₂, 1 mM CaCl₂, 1% NP-40, 10% glycerol, with protease and phosphatase inhibitors, and 12.5 U ml⁻¹ benzonase (Novagen, 70746).

Bacterial expression and GST pulldown. GST-tagged ETS2 constructs were transformed and expressed in BL21-CodonPlus *E. coli*. Bacterial lysates were incubated with glutathione beads (Life Technologies, number G2879) at 4 °C for 2 h, and washed four times with buffer containing 50 mM Tris, pH 7.5, 150 mM NaCl, 1% Triton, 1 mM DTT, supplemented with 100 µM PMSF. The *in vitro* translated (Thermo, number 88881) HA-tagged wild-type p53 or GOF p53 proteins were pre-cleared with GST at 4 °C for 1 h and the resulting supernatant was subjected to GST pulldown with GST or GST-ETS2. The product was then washed and subjected to western blot analysis.

RT-qPCR, ChIP-qPCR and ChIP-sequencing. RNA was isolated from cells using RNeasy kit (Qiagen, number 74106). RNA was then reverse transcribed to cDNA (Life Technologies, number 4387406), then qPCR was performed for quantification using standard procedures on a 7900HT Fast-Real-Time PCR platform (ABI). ChIP was performed as previously described⁴⁰, with modifications. In brief, cells were crosslinked in 1% formaldehyde (Thermo, number 28906) in PBS for 10 min at room temperature. After glycine quenching, cell pellets were collected and lysed as previously described⁴⁰, and then subjected to sonication with the Covaris sonicator (S220). The supernatant was then diluted in the same sonication buffer but without *N*-lauroylsarcosine, and subjected to immunoprecipitation with corresponding antibodies at 4 °C overnight. The beads were then washed and DNA was reverse-crosslinked and purified. Following ChIP, DNA was quantified by qPCR using standard procedures on a 7900HT Fast-Real-Time PCR platform (ABI), or sequencing libraries were prepared using NEBNext Ultra library preparation procedure, and then sequenced on Illumina Hi-Seq platform at the Next-Generation Sequence Core at University of Pennsylvania, or on Illumina Next-Seq platform in the Epigenetics Program at the University of Pennsylvania. All primer sequences used in this study are available in Supplementary Table 3.

Growth curve measurement. 200,000 cells were seeded on 950 mm² surface area (one well of 6-well plate) on day 0. Cell number was measured every two days with

Countess automated cell counter (Life Technologies) following standard procedures and default parameter settings, after which 200,000 cells were plated back for the next count. For shRNA-mediated knockdown experiments, cells were seeded 7 days after the initial infection of shRNA-containing lentivirus, during which puromycin selection was completed and cells were returned to normal growth medium. For small compound inhibitor treatment experiments, inhibitors or DMSO vehicle control were added on day 0 as cells were seeded, and refreshed every other day as cells were counted and replated. All short hairpin sequences used in this study are available in Supplementary Table 3.

Colony-formation assay. After lentiviral infection of shRNA constructs and puromycin selection, 2,000 cells were seeded per well in 6-well plates. After three weeks, cell colonies were fixed with 1% paraformaldehyde and stained with 0.1% crystal violet (for 15 min). For quantification, the crystal violet dye was released into 10% acetic acid and measured at $A_{590\text{nm}}$ (OD590).

Soft agar anchorage-independent growth assay. The base layer of soft agar contained complete DMEM media (10% FBS, 100 units per ml penicillin and 100 µg per ml streptomycin) with 1% agar; the top layer of soft agar contained complete DMEM media with 0.7% agarose and was mixed with 5,000 cells and plated over the base layer. Colonies were fixed and stained with 0.005% crystal violet (for 1 h), and visible colonies were counted.

Tumour xenograft assay. A total of four male and four female mice (*Mus musculus*, strain NOD.Cg-Prkdc^{scid} Il2rg^{tm1Wjl}/SzJ, Jackson Labs (stock number 005557)) between the ages of 38 and 45 days old were used per treatment for tumour xenograft experiments. All animal experiments described adhere to policies and practices approved by the University of Pennsylvania Institutional Biosafety Committee (IBC) and the Institutional Animal Care and Use Committee (IACUC). Cells were collected after shRNA (MLL1 or non-targeting control) mediated knockdowns. Then 1.5 million cells were injected subcutaneously per mouse. Tumour size was measured by calipers 10 weeks after subcutaneous injection. Tumour size was measured in two dimensions, and tumour volume was calculated as $0.5 \times \text{length} \times \text{width}^2$. All mice were euthanized 20 weeks after subcutaneous injection. Tumours were then excised and photographed.

ChIP-sequencing and RNA-sequencing analysis. Human cell sequencing reads were aligned to human genome hg18 using Bowtie2 (ref. 41). For p53 ChIP-seq, significant regions of enrichment (peaks) were called using HOMER (Salk Institute, <http://homer.salk.edu>). For area under the curve analysis, ChIP-seq tags from each cell line were counted at TSS proximal peaks (200 bp around peak centres) of every cell line (including itself) as indicated. Heat maps of p53 enrichment across a 5 kb region (± 2.5 kb from peak centre, bin = 10) in MCF7, MDA-MB-175VII, MDA-MB-468, HCC70, BT-549 cell lines were generated using HOMER and visualized using JavaTreeView. Sequencing reads from MEFs ChIP-seq experiments were aligned to the mouse reference genome mm9 using Bowtie2. Strand-specific mouse RNA-seq experiments were aligned to the mm9 reference genome and reference transcriptome. FPKM expression values were counted for each exon and merged into a single gene model using HOMER.

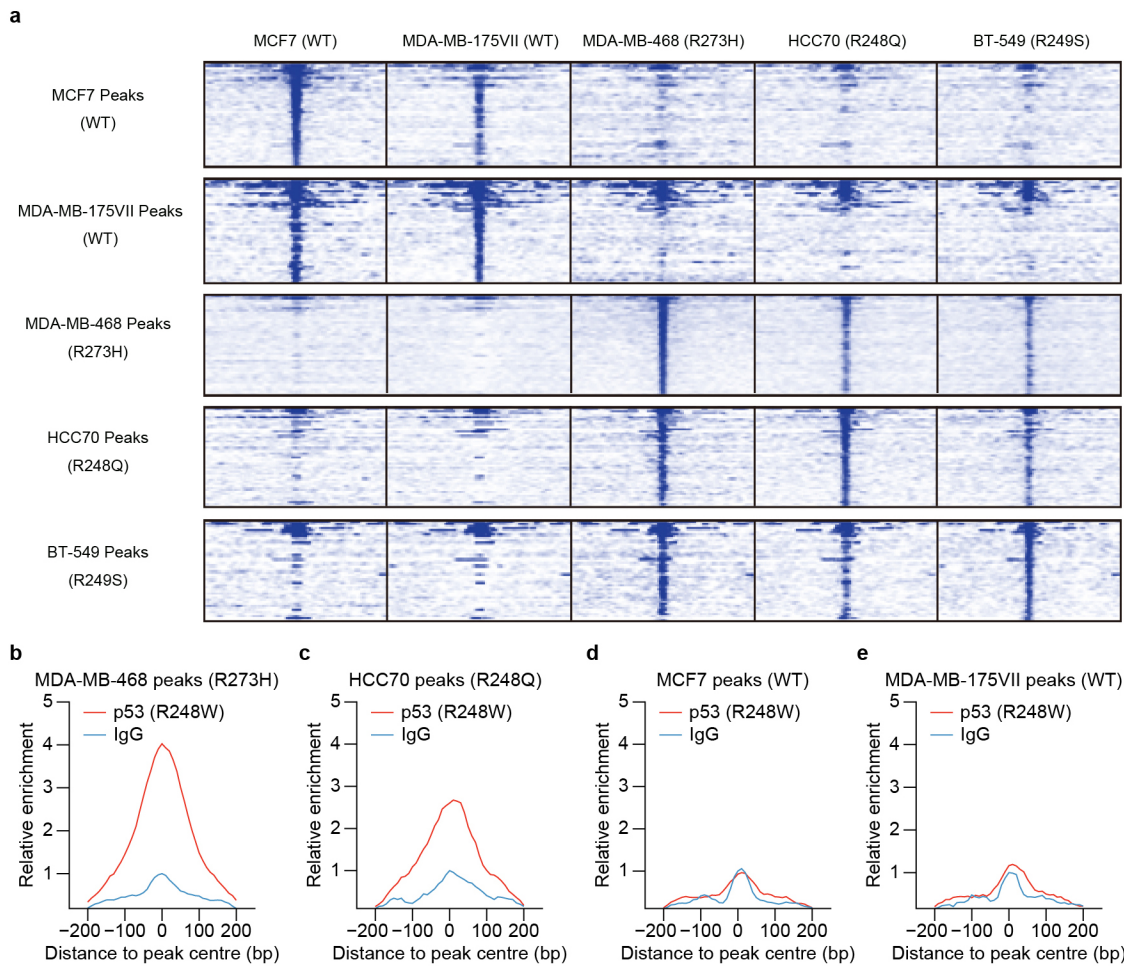
Motif analysis. To determine associated sequence motifs for wild-type p53 or GOF p53 peaks, all TSS proximal peaks (filtered to remove peaks overlapping with satellite DNA) were pared down to the central 50 bp and used as input to MEME and the SeqPos utility in Cistrome (central 100 bp as required by SeqPos). MEME was instructed to search for the top 10 motifs appearing 0 or more times in each sequence, and SeqPos was run with default parameters.

Gene ontology analysis. GO terms associated with wild-type p53 or GOF p53 binding sites were determined in the following way. ChIP-seq TSS proximal peaks were associated with the nearest ENSEMBL transcript and processed using DAVID. The FDR was controlled at 1% and GO terms with fewer than 5 associated transcripts or a fold-enrichment over the genomic background under fivefold were discarded.

Intersection with ENCODE transcription factor data sets. Transcription factor peak coordinates (hg18 assembly) were obtained from the ENCODE project repository (<http://www.encodeproject.org>) in BED format. TSS proximal p53 ChIP-seq peak regions were intersected with all transcription factor binding-site data using BEDTools, with overlap inferred if a minimum of a single base pair was in common.

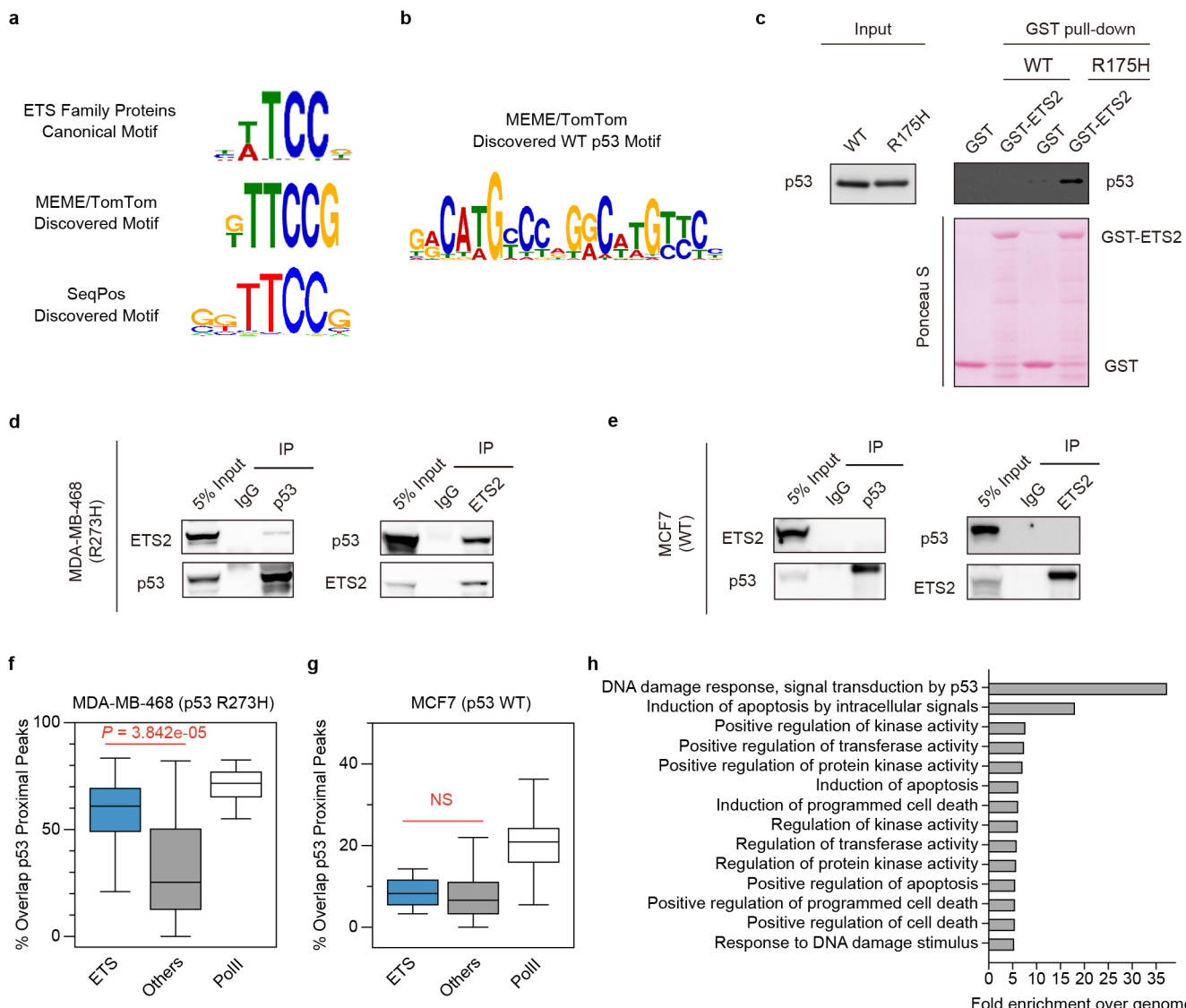
TCGA analysis. Exome sequencing and RNA sequencing data sets were obtained from TCGA (<https://tcga-data.nci.nih.gov/tcga/>). Based on p53 mutational status from the exome sequencing data sets, we grouped tumour samples into: (1) wild type (tumours without detectable p53 mutation); (2) GOF (tumours with p53 single missense mutation of R175H, R248Q, R248W, R249S or R273H); and (3) null (tumours with p53 nonsense mutations or frameshift truncations). Tumours with other types of p53 mutations (other missense mutations, inframe insertion/deletion, or splicing mutations) were not included in further analysis, due to an unpredictable effect on the downstream chromatin regulators. Cancer types that include more than 5% samples in group 2 were included for the combined analysis, in which RNA expression values were normalized to the wild-type group

- median. For individual cancer type analysis, original RNA expression values (normalized read counts or RPKM values) from TCGA data sets were used.
- OICR-9429.** OICR-9429 was developed using structure-guided medicinal chemistry and peptide displacement assays starting from ‘Compound 3’ previously reported in ref. 42, as part of the Chemical Probe Program of the Structural Genomics Consortium. OICR-9429 is highly specific for WDR5 and was shown to have >100-fold selectivity over 300 other chromatin ‘reader’ domains, methyl-transferases, and other non-epigenetic targets. The details of its structure, discovery and characterization are described in ref. 38.
39. Lee, K. H. *et al.* A genome-wide study identifies the Wnt signaling pathway as a major target of p53 in murine embryonic stem cells. *Proc. Natl Acad. Sci. USA* **107**, 69–74 (2010).
 40. Shah, P. P. *et al.* Lamin B1 depletion in senescent cells triggers large-scale changes in gene expression and the chromatin landscape. *Genes Dev.* **27**, 1787–1799 (2013).
 41. Langmead, B. & Salzberg, S. L. Fast gapped-read alignment with Bowtie 2. *Nature Methods* **9**, 357–359 (2012).
 42. Senisterra, G. *et al.* Small-molecule inhibition of MLL activity by disruption of its interaction with WDR5. *Biochem. J.* **449**, 151–159 (2013).



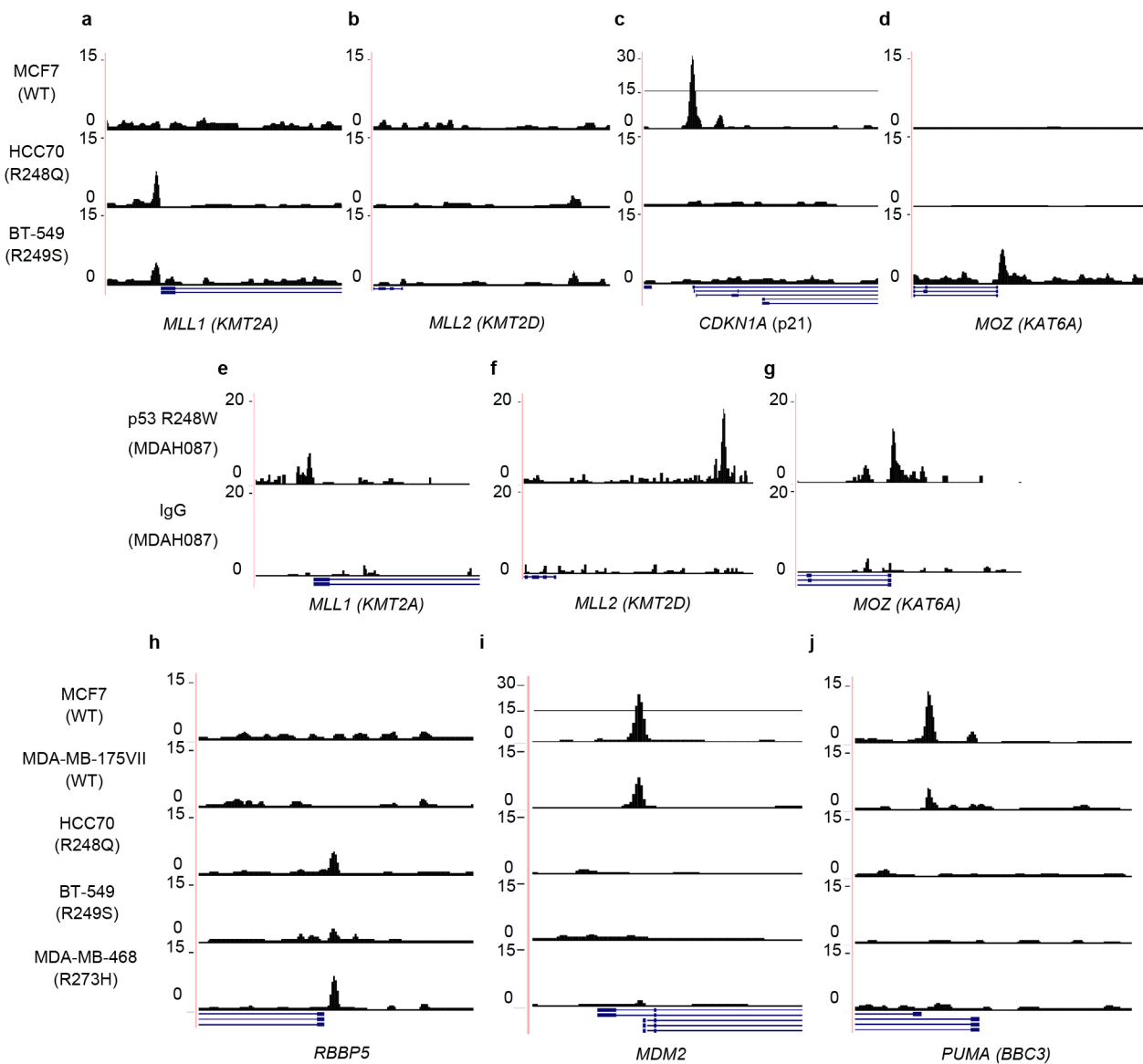
Extended Data Figure 1 | Distinct GOF p53 mutants have similar genome-wide binding patterns, but are different from that of wild-type p53. **a**, Heat maps showing the enrichment of p53 peaks ($\pm 2,500$ bp around peak centre) identified from each cell line (rows) in all five cell lines (columns) examined by

ChIP-seq. **b–e**, Area under the curve, meta-peak analysis showing GOF p53(R248W) or IgG ChIP-seq signal enrichment from MDAH087 cells over TSS-proximal peaks identified in MDA-MB-468 (**b**), HCC70 (**c**), MCF7 (**d**) and MDA-MB-175VII (**e**) cells.



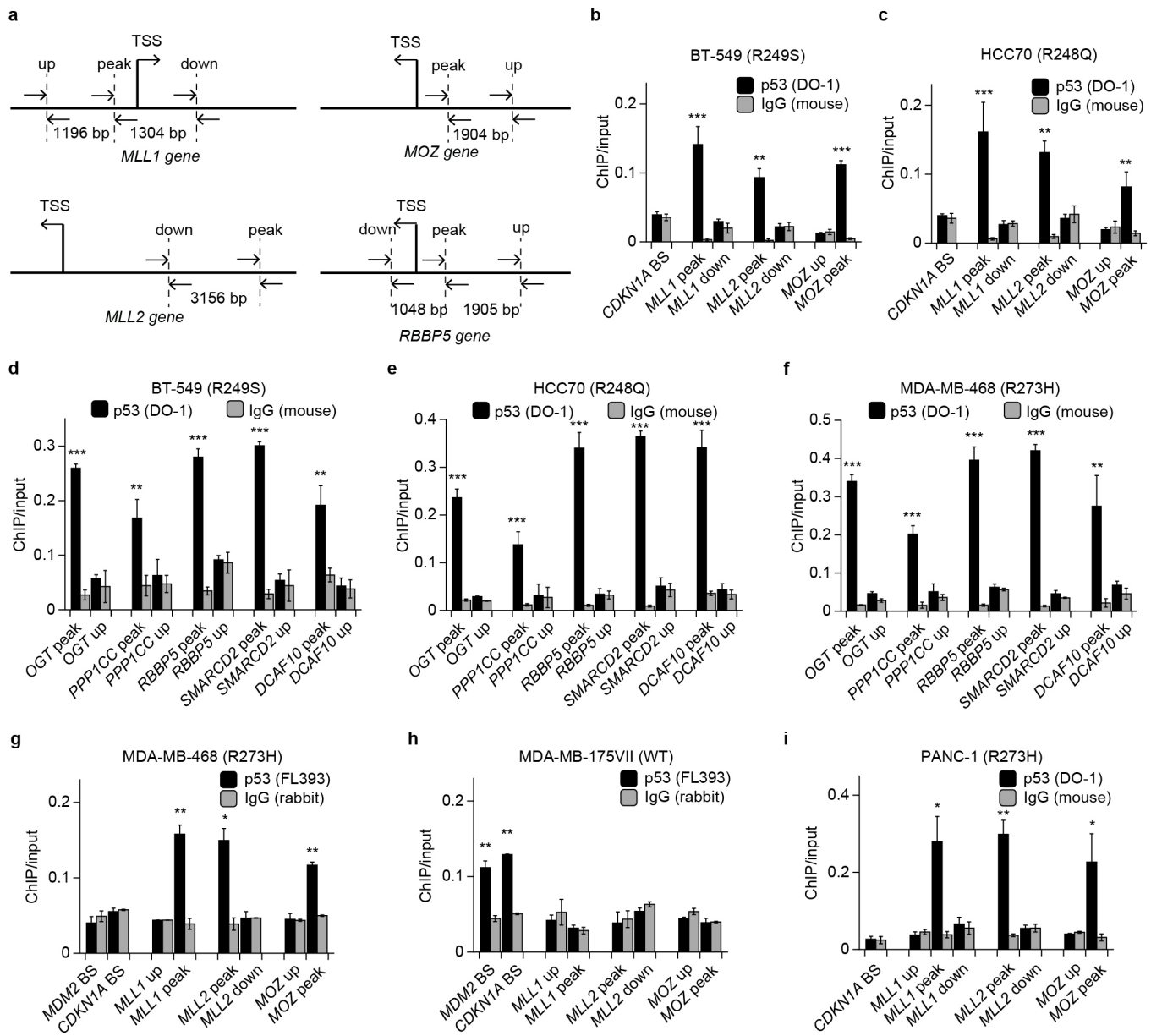
Extended Data Figure 2 | GOF p53 genome-wide binding is in association with ETS family proteins. **a**, Canonical ETS binding motif (top), and discovered motif from all TSS-proximal peaks in MDA-MB-468 predicted by MEME/TomTom (middle), or SeqPos (bottom). **b**, MEME/TomTom identified wild-type p53 motif from MDA-MB-175VII TSS-proximal peaks. **c**, GST pulldown of bacterially expressed GST or GST-ETS2 with *in vitro* translated wild-type p53 or p53(R175H). **d, e**, Co-immunoprecipitation at endogenous protein levels of ETS2 and GOF p53(R273H) (**d**) or wild-type p53

(**e**) in MDA-MB-468 (**d**) or MCF7 (**e**) cells. **f, g**, Box plots showing overlap of GOF p53 TSS-proximal peaks from MDA-MB-468 cells or wild-type p53 (**g**) TSS-proximal peaks from MCF7 cells, with ETS family proteins (blue), all other transcription factors (grey) or Pol II (white) peaks from ENCODE ChIP-seq data sets. Whiskers on the box plots represent the inter-quartile range. Mann-Whitney *U*-tests were performed to compute significance. **h**, GO analysis of wild-type p53 TSS-proximal peaks (statistics are shown in Supplementary Table 1).



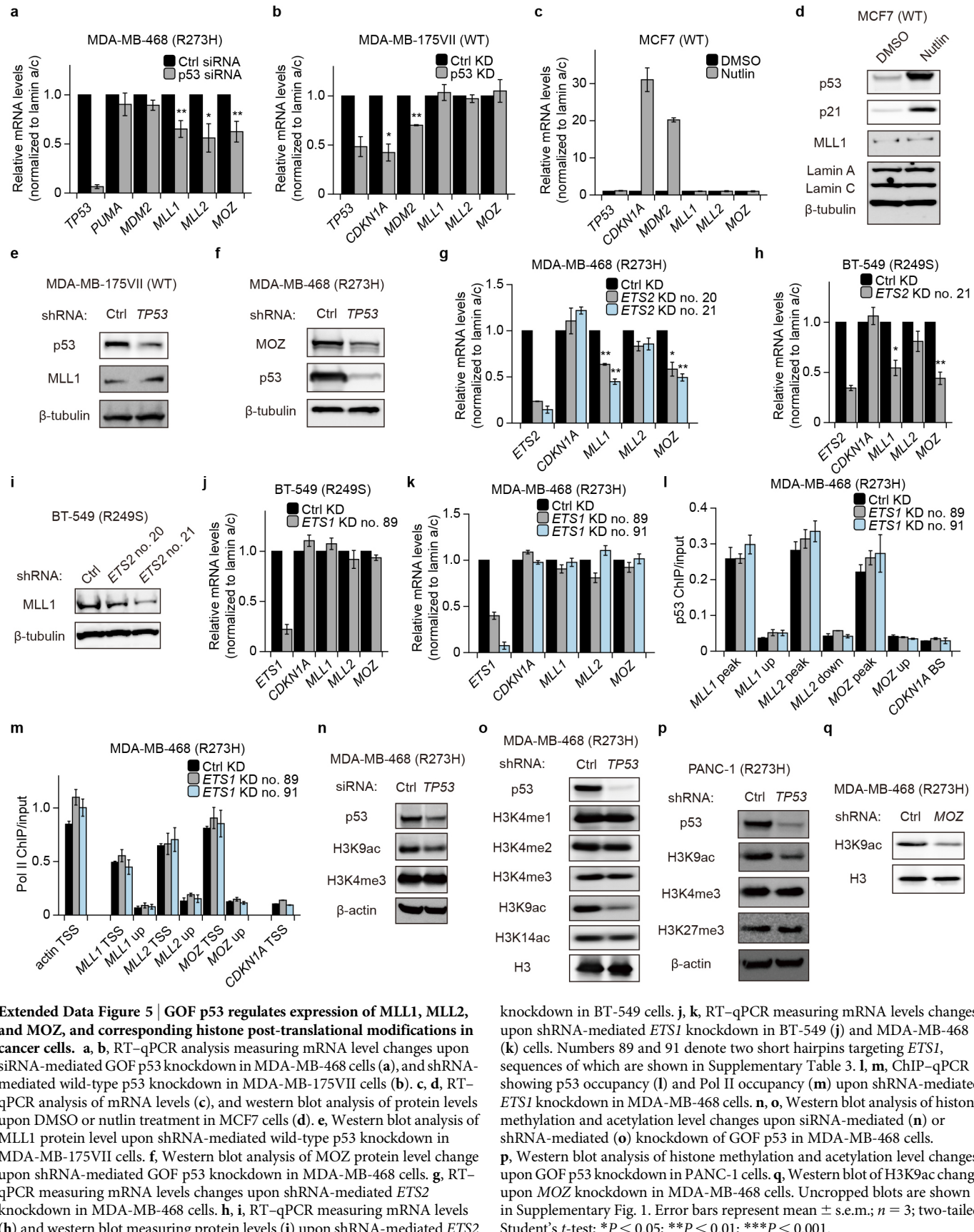
Extended Data Figure 3 | UCSC Genome Browser views showing distinct wild-type p53 and GOF p53 binding patterns over representative canonical wild-type p53 targets and novel GOF p53 targets. a-d, UCSC Genome Browser views of p53 occupancy over promoter regions of *MLL1* (a), *MLL2* (b), *CDKN1A* (c) and *MOZ* (d) in MCF7, HCC70, and BT-549 cells.

e-g, Re-aligned GOF p53(R248W) and IgG ChIP-seq data from LFS MDAH087 cells, showing enrichment of GOF p53 at promoter regions of *MLL1* (e), *MLL2* (f), and *MOZ* (g). h-j, UCSC Genome Browser views of p53 occupancy over promoter regions of *RBBP5* (h), *MDM2* (i) and *PUMA* (j), in MCF7, MDA-MB-175VII, HCC70, BT-549, and MDA-MB-468 cells.



Extended Data Figure 4 | ChIP-qPCR validation of GOF p53 binding at newly identified chromatin regulator genes. **a**, Schematic of amplicon locations for ChIP-qPCR validations performed in this study. **b, c**, ChIP-qPCR showing p53 (DO-1 antibody) or IgG (mouse) enrichment (ChIP/input) over *MLL1*, *MLL2* and *MOZ* peak regions, in BT-549 (**b**) and HCC70 (**c**) cells. **d–f**, ChIP-qPCR showing p53 (DO-1 antibody) or IgG (mouse) enrichment over OGT, PPP1CC, RBBP5, SMARCD2, and DCAF10 peak regions in BT-549

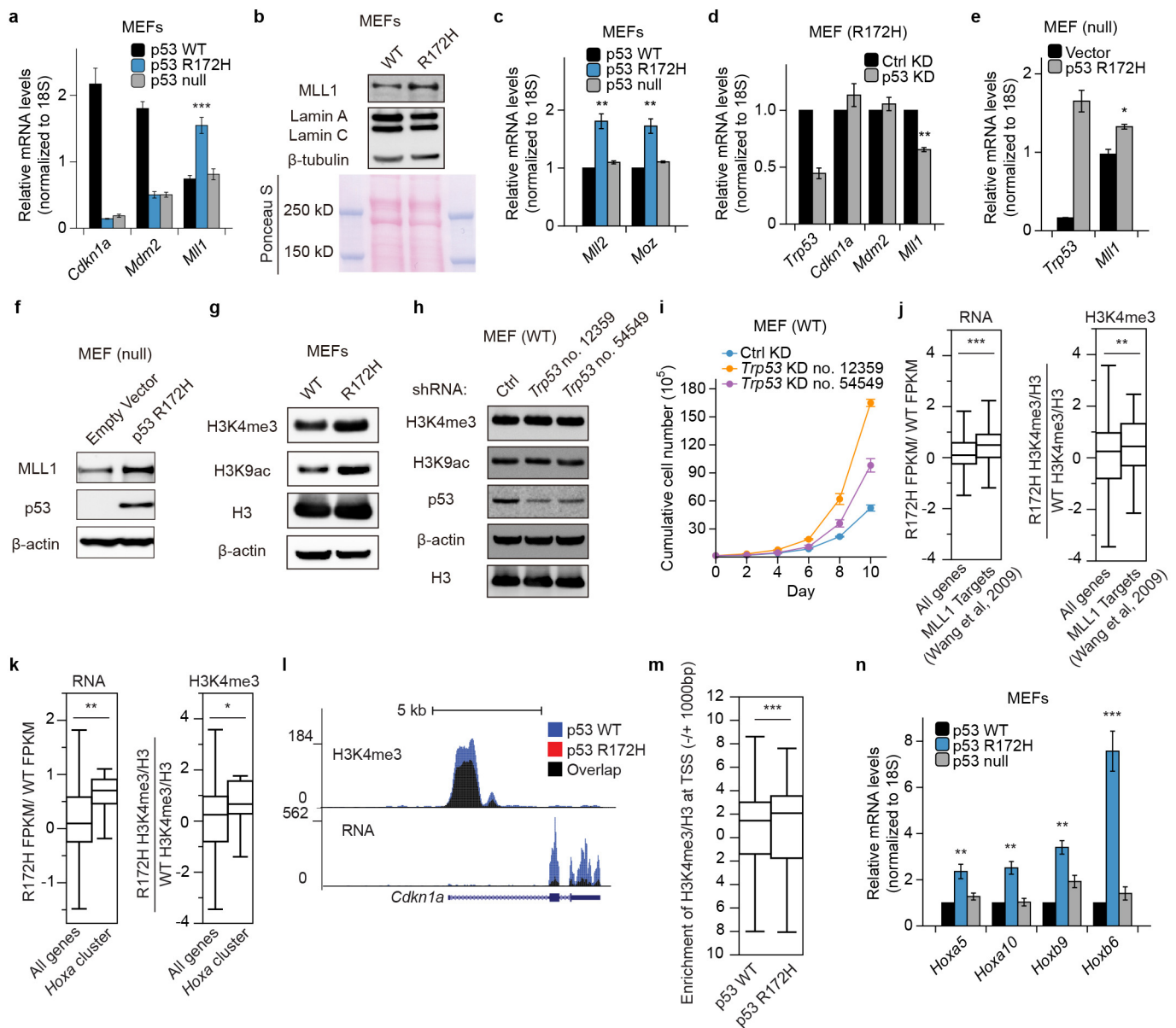
(**d**), HCC70 (**e**) and MDA-MB-468 (**f**) cells. **g, h**, ChIP-qPCR showing p53 (FL393 antibody) or IgG (rabbit) enrichment over *MDM2*, *CDKN1A*, *MLL1*, *MLL2* and *MOZ* regions, in MDA-MB-468 (**g**) and MDA-MB-175VII (**h**) cells. **i**, ChIP-qPCR showing p53 (DO-1 antibody) or IgG (mouse) enrichment over *MLL1*, *MLL2* and *MOZ* peak regions in PANC-1 cells. Error bars represent mean \pm s.e.m.; $n = 3$; two-tailed Student's *t*-test: * $P < 0.05$; ** $P < 0.01$; *** $P < 0.001$.



Extended Data Figure 5 | GOF p53 regulates expression of MLL1, MLL2, and MOZ, and corresponding histone post-translational modifications in cancer cells. **a**, **b**, RT-qPCR analysis measuring mRNA level changes upon siRNA-mediated GOF p53 knockdown in MDA-MB-468 cells (**a**), and shRNA-mediated wild-type p53 knockdown in MDA-MB-175VII cells (**b**). **c**, **d**, RT-qPCR analysis of mRNA levels (**c**), and western blot analysis of protein levels upon DMSO or nutlin treatment in MCF7 cells (**d**). **e**, Western blot analysis of MLL1 protein level upon shRNA-mediated wild-type p53 knockdown in MDA-MB-175VII cells. **f**, Western blot analysis of MOZ protein level change upon shRNA-mediated GOF p53 knockdown in MDA-MB-468 cells. **g**, RT-qPCR measuring mRNA levels changes upon shRNA-mediated ETS2 knockdown in MDA-MB-468 cells. **h**, **i**, RT-qPCR measuring mRNA levels (**h**) and western blot measuring protein levels (**i**) upon shRNA-mediated ETS2

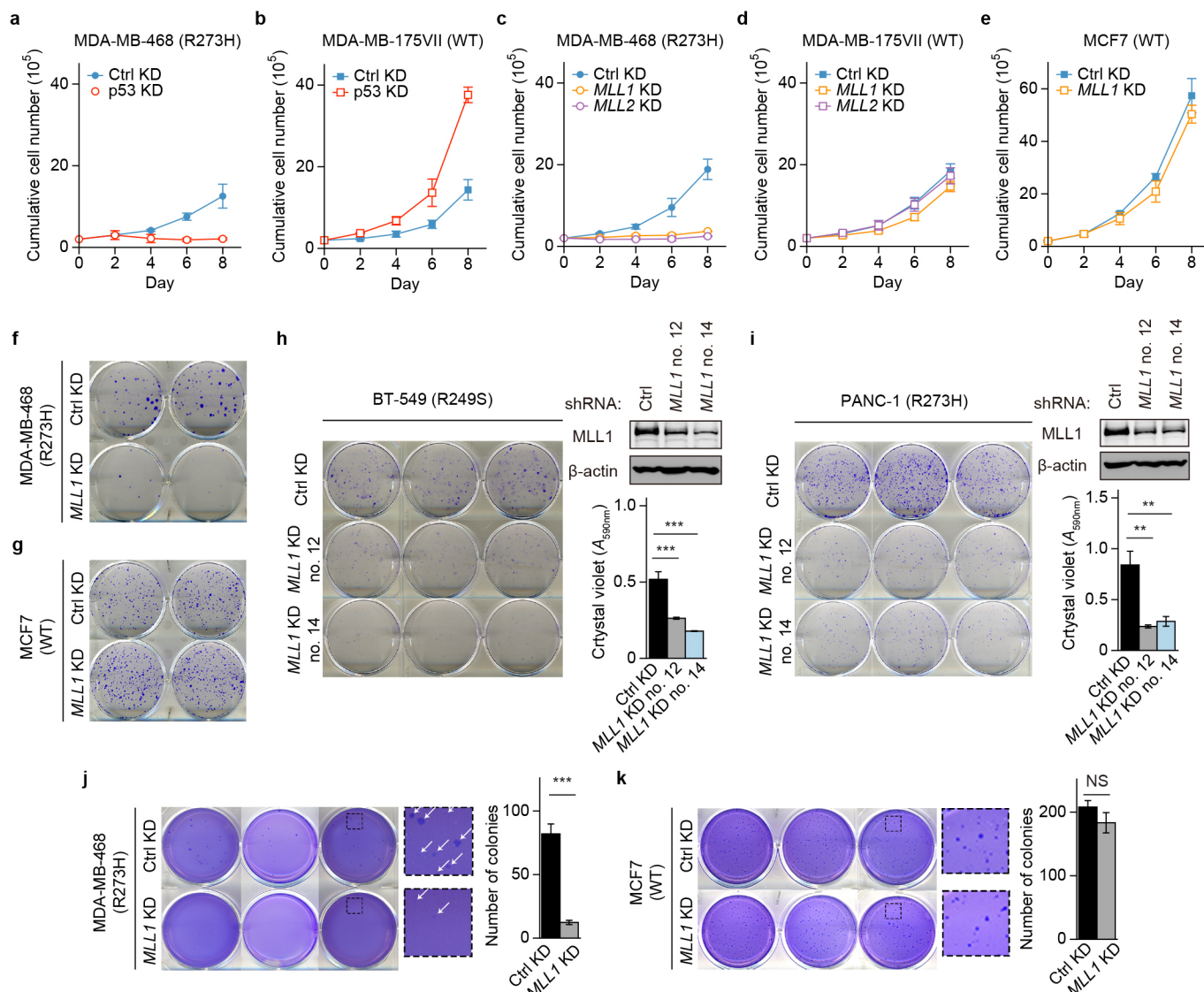
knockdown in BT-549 cells. **j**, **k**, RT-qPCR measuring mRNA levels changes upon shRNA-mediated ETS1 knockdown in BT-549 (**j**) and MDA-MB-468 (**k**) cells. Numbers 89 and 91 denote two short hairpins targeting ETS1, sequences of which are shown in Supplementary Table 3. **l**, **m**, ChIP-qPCR showing p53 occupancy (**l**) and Pol II occupancy (**m**) upon shRNA-mediated ETS1 knockdown in MDA-MB-468 cells. **n**, **o**, Western blot analysis of histone methylation and acetylation level changes upon siRNA-mediated (**n**) or shRNA-mediated (**o**) knockdown of GOF p53 in MDA-MB-468 cells.

p, Western blot analysis of histone methylation and acetylation level changes upon GOF p53 knockdown in PANC-1 cells. **q**, Western blot of H3K9ac change upon MOZ knockdown in MDA-MB-468 cells. Uncropped blots are shown in Supplementary Fig. 1. Error bars represent mean \pm s.e.m.; $n = 3$; two-tailed Student's *t*-test; * $P < 0.05$; ** $P < 0.01$; *** $P < 0.001$.



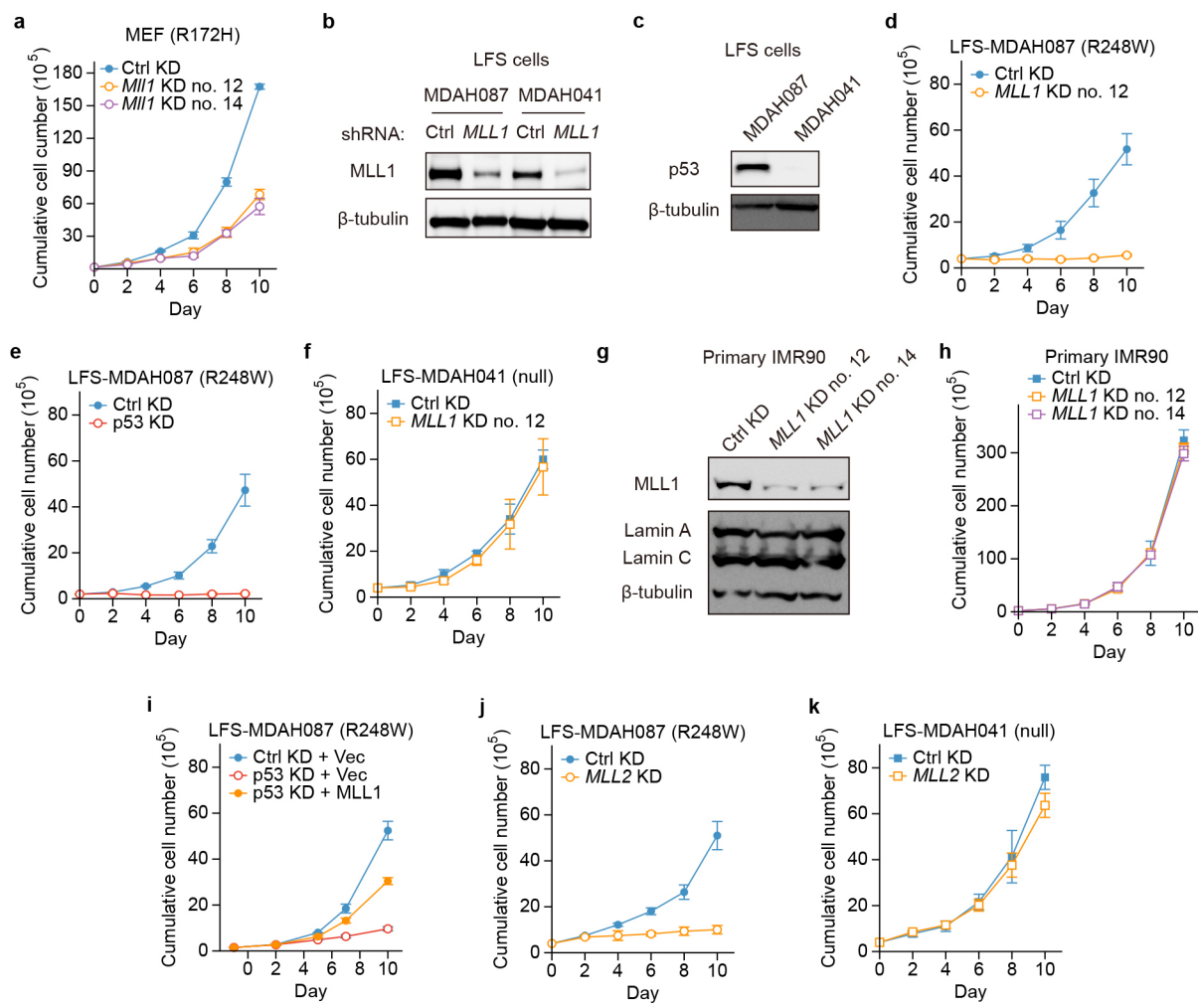
Extended Data Figure 6 | GOF p53 regulates expression of Mll1, Mll2, and corresponding histone post-translational modifications in primary MEFs. **a**, RT-qPCR analysis comparing *Mll1* expression levels between MEFs bearing wild-type p53, GOF p53(R172H), and p53 null. **b**, Western blot comparing Mll1 protein level between MEFs with wild-type p53 and GOF p53. **c**, RT-qPCR analysis comparing *Mll2* and *Moz* expression levels between MEFs bearing wild-type p53, GOF p53(R172H), and p53 null. **d**, RT-qPCR measuring mRNA changes upon shRNA-mediated p53 knockdown in GOF p53(R172H) knock-in MEFs. **e**, **f**, RT-qPCR analysis of mRNA levels (**e**) and western blot of protein levels (**f**) upon retroviral expression of GOF p53(R172H) in MEFs with p53 knockout. **g**, Western blot comparing H3K4me3 and H3K9ac levels between MEFs with wild-type p53 and GOF p53(R172H). **h**, Western blot showing H3K4me3 and H3K9ac levels upon p53 knockdown in wild-type p53 MEFs. **i**, Growth curve analysis of wild-type p53 MEF proliferation upon shRNA-mediated p53 knockdown. **j**, **k**, Box plot analysis of RNA levels (left) and H3 normalized H3K4me3 levels

(right) at previously discovered *Mll1* target genes (**j**) or *Hoxa* cluster genes (**k**) compared with all genes, from RNA-seq and H3K4me3 ChIP-seq in MEFs with wild-type p53 or GOF p53 R172H. Plots are presented as ratios of GOF p53(R172H) values over wild-type p53 values. **l**, UCSC Genome Browser views of H3K4me3 enrichment (top) and RNA levels (bottom) of *Cdkn1a*, from H3K4me3 ChIP-seq and RNA-seq of MEFs with wild-type p53 or GOF p53(R172H). Tracks are presented as overlay of wild-type p53 and GOF p53 signals. Blue denotes more enriched in wild-type p53, red denotes more enriched in GOF p53(R172H), black denotes overlap. **m**, Box plot of H3 normalized H3K4me3 levels over all gene TSSs, from H3K4me3 ChIP-seq in MEFs with wild-type p53 or GOF p53(R172H). **n**, RT-qPCR analysis comparing *Hox* gene expression levels between MEFs bearing wild-type p53, GOF p53(R172H), and p53 null. Uncropped blots are shown in Supplementary Fig. 1. For all bar graphs, two-tailed Student's *t*-test; **P* < 0.05; ***P* < 0.01; ****P* < 0.001. Error bars represent mean ± s.e.m.; *n* = 3. For all box plots, Mann-Whitney U-test; **P* < 0.05; ***P* < 0.01; ****P* < 0.001.



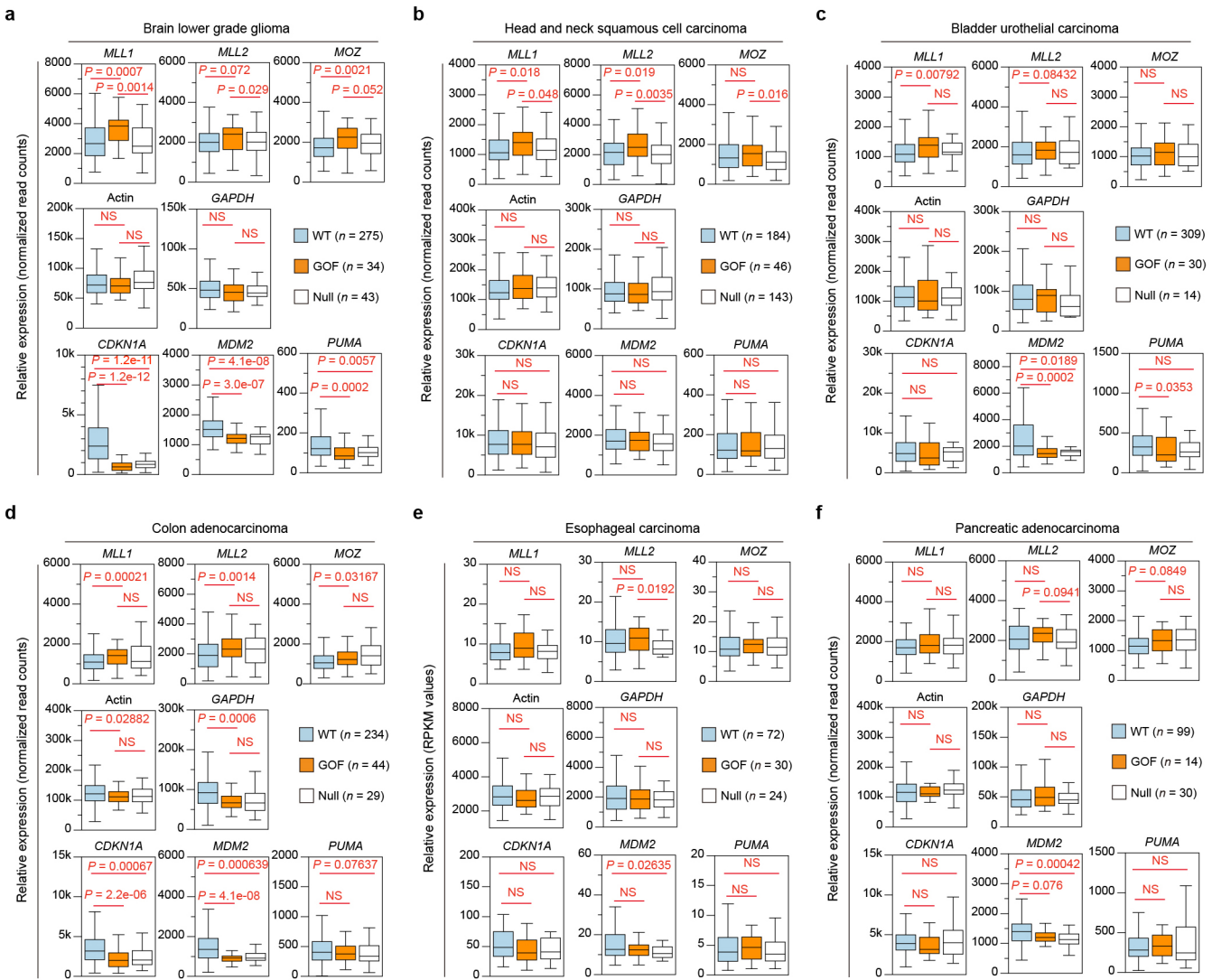
Extended Data Figure 7 | MLL knockdown reduces proliferation and cancer phenotype specifically in GOF p53 cancer cells. **a, b,** Growth curve analysis of MDA-MB-468 (**a**) and MDA-MB-175VII (**b**) cells with either non-targeting control shRNA or p53 shRNA knockdown. **c, d,** Growth curve analysis of MDA-MB-468 (**c**) and MDA-MB-175VII (**d**) cells with non-targeting control shRNA, *MLL1* shRNA, or *MLL2* shRNA knockdown. **e,** Growth curve analysis of MCF7 cells with non-targeting control shRNA or *MLL1* shRNA knockdown. **f, g,** Colony-formation assay of MDA-MB-468 (**f**) and MCF7 (**g**) cells with either non-targeting control shRNA or *MLL1* shRNA knockdown. Corresponding to Fig. 4a, b. **h, i,** Colony-formation assay of

BT-549 (**h**) and PANC-1 (**i**) cells with either non-targeting control shRNA or two different *MLL1* shRNA knockdown, and quantification by crystal violet staining over three biological replicates. Reduction of *MLL1* protein is also shown by western blot. **j, k,** Anchorage-independent soft agar assay of MDA-MB-468 (**j**) and MCF7 (**k**) cells with either non-targeting control shRNA or *MLL1* shRNA knockdown. Dashed boxes denote enlarged images of the selected areas. White arrows indicate visible colonies in **j**. Quantifications are shown as number of visible colonies. Error bars represent mean \pm s.e.m.; $n = 3$; two-tailed Student's *t*-test; ** $P < 0.01$; *** $P < 0.001$.



Extended Data Figure 8 | MLL knockdown reduces proliferation specifically of GOF p53 MEFs and LFS cells. **a**, Growth curve analysis of GOF p53(R172H) MEFs with either non-targeting control shRNA or two different *Mll1* shRNA knockdowns. **b**, Western blot analysis of MLL1 levels upon shRNA-mediated knockdown in LFS MDAH087 and MDAH041 cells. **c**, Western blot analysis of p53 protein levels in LFS MDAH087 and MDAH041 cells. **d**, **e**, Growth curve analysis of LFS MDAH087 cells upon *MLL1* (d) knockdown or p53 (e) knockdown. **f**, Growth curve analysis of LFS

MDAH041 cells upon *MLL1* knockdown. **g**, **h**, Western blot analysis of MLL1 level (g) and growth curve analysis (h) of proliferation upon shRNA-mediated *MLL1* knockdown in IMR90 cells. **i**, Growth curve analysis of LFS MDAH087 cells with non-targeting control shRNA plus empty vector, p53 shRNA plus vector, and p53 shRNA plus MLL1 expressing vector. **j**, **k**, Growth curve analysis of LFS MDAH087 (j) and LFS MDAH041 (k) cells with either non-targeting control shRNA or *MLL2* shRNA knockdown.



Extended Data Figure 9 | TCGA RNA expression profile analysis. a–f, TCGA RNA expression profile of GOF p53 target genes (top), housekeeping genes (middle), and wild-type p53 target genes (bottom) in brain lower grade glioma (a), head and neck squamous cell carcinoma (b), bladder urothelial carcinoma (c), colon adenocarcinoma (d), oesophageal

carcinoma (e) or pancreatic adenocarcinoma tumours (f) with wild-type p53 (blue), GOF p53 (orange), or p53 null (white). Expression values are normalized read counts (a–d, f), or RPKM values (e) from TCGA RNA-seq data sets. Mann–Whitney *U*-tests were performed to compute significance.